Atom cloud compression in a 3D optical lattice and laser intensity stabilisation using an in-house developed photodiode amplifier

Muhib Omar

I hereby declare that this thesis was formulated by myself and that no sources or tools other than those cited were used.

Bonn, ...
                    Date   Signature

1. Gutachter: Prof. Dr. Dieter Meschede
2. Gutachter: Prof. Dr. Stefan Linden

1 INTRODUCTION

1.1 Motivation

Quantum information is arguably one of the most promising fields of physics which could affect everyday life fundamentally in the future. The introductory quantum mechanic course's postulate that a measurement always changes the quantum mechanical state has been exploited in the emerging industrial method of quantum cryptography[1]. Algorithms like Shor's discrete logarithm and integer factorisation [2] on the other hand may due to exploiting quantum mechanical interference effects be implemented on a quantum computer outperforming classical algorithms performed on classical computers in efficiency.

Our group's 2D Discrete Quantum Simulator (DQSIM) experiment is dedicated to the idea of a discrete time quantum walk. A quantum walk is the quantum mechanical analogue of a classical random walk[3]. Discrete refers here to the timing in which evolution operators are applied to two quantum systems, a walker and a coin. It not only exhibits different statistics than the classical counterpart but may be employed in a multitude of ways. For example the experimental simulation of a perfect conductor in which Bloch oscillations are performed [4] or the simulation of topological systems that are otherwise inaccessible in solid state physical scales[5].

1.2 Outline

The next chapter reviews the DQSIM setup and necessary concepts to assess the place the content of the thesis is going to take within the experimental effort of our group. Then this thesis deals with two additions to the DQSIM experiment. The first part concerns a specifically designed photodiode amplifier circuit to improve the intensity stabilisation of the lattice beams.

Improving it would ensure that the coherence time of the atoms isn't limited by intensity noise any more.

The second part introduces a scheme to realise compression of atomic ensembles trapped in our optical lattice. Furthermore it is a first step in achieving an efficient single plane selection and addressing in our experiment opening the door to many-particle quantum walks like [6]. The thesis concludes with a discussion about initial experimental attempts on compression and a summary of the results.

2 DQSIM EXPERIMENTAL SETUP

In this chapter, an overview of the experimental main apparatus and techniques will be presented. This is followed by a description of the trapping and cooling techniques and then will conclude in an overview of the limitations this thesis aims to address.

2.1 DQSIM setup

State-dependent transport of neutral atoms is realised in our experiment by a polarisation-synthesized two dimensional optical lattice potential. Its potential is nearly independently acting on ^{137}Cs atoms prepared in one of two spin states.
The state preparation is achieved by optical pumping into the $|\uparrow\rangle = |F = 4, m_F = 4\rangle$ hyperfine polarisation state after applying a magnetic field gradient to lift the degeneracy of its hyperfine states. $|\uparrow\rangle$ is coupled by pulsed microwave radiation at a frequency of about 9.2 GHz with the $|\downarrow\rangle = |F = 3, m_F = 3\rangle$ state [8, p.34], see Fig.2.1
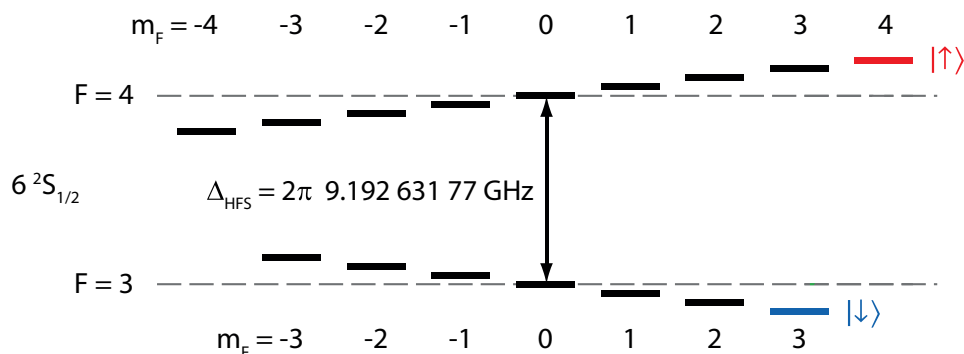

Figure 2.1: Level scheme of Cs after applying a magnetic field[9, p.5].

Those two states form an effective two level system.

The beam configuration generating the state sensitive potential is shortly reviewed in Fig. 2.2a and Fig. 2.2b :
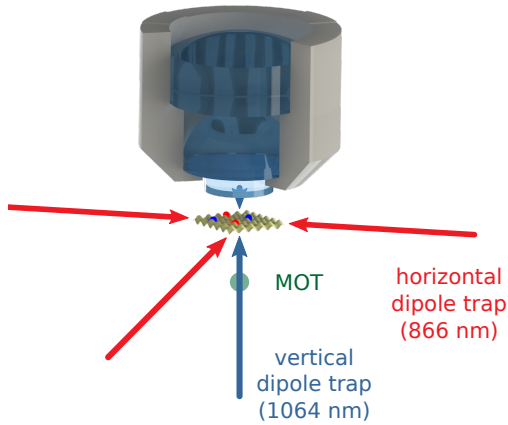
2.2 a) Sketch of the beam configuration for the state dependent horizontal dipole potential trap (HDT,red). Perpendicular to it the vertical dipole beam (VDT,blue) is retroreflected by the high numerical aperture (NA) objective forming a standing wave pattern. The position of the MOT before loading atoms into the lattice is marked. Sketch not up to scale [7, p.43].
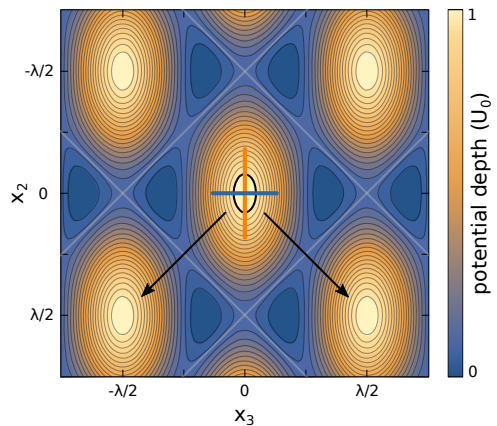
2.2 b) HDT potential contour plot. The colour indicates the trap depth normalised by the maximal trap depth. The vertical plot axis is parallel to the counterpropagating beams. The horizontal axis parallel to the perpendicular HDT beam. The black arrows indicate the transport direction achieved by steering the polarisation phase of the counterpropagating beams. Image taken from [7, p.74].

The counterpropagating horizontal dipole trap (HDT) beams are linear polarised, consisting of two independently tunable circular polarisation components. The orthogonal horizontal beam, is of a fixed linear polarisation. All combined are used to create a state-dependent 2 dimensional optical lattice. The vertical dipole trap (VDT) beams are for the purpose of confining the atoms in the HDT plane. Their tighter confinement is in addition advantageous for achieving ground state cooling along its direction. It also enhance the imaging due to confining the atoms within the depth of focus of the vertical lattice spacing. The reason lies in its lattice constant of $0.5\,\mu\text{m}$ being smaller than the depth of focus of the high NA (0.92) objective of $10\,\mu\text{m}$[7, p.41].

Choosing the HDT beam wavelength to be 865.8 nm the resulting lattice potential $U_{\uparrow,\downarrow}$ acts nearly independently on $|\uparrow\rangle$ and $|\downarrow\rangle$ with its σ^+ and σ^- beam polarisation [7, p.69]:

$$\begin{pmatrix} U_\uparrow \\ U_\downarrow \end{pmatrix} = k \begin{pmatrix} 1 & 0 & 1/2 \\ 1/8 & 7/8 & 1/2 \end{pmatrix} \cdot \begin{pmatrix} I_{\sigma^+} \\ I_{\sigma^-} \\ I_\pi \end{pmatrix} \tag{2.1}$$

with $k = -k_B\,2.717\,\text{pK}/(\text{W/m}^2)$ and k_B the Boltzmann constant. The atoms are attracted to the intensity maxima of the corresponding potential due to being red detuned in this case.

The coefficients of each beam polarisation component contributing to the potential of either hyperfine state are determined by calculating the AC-Stark shift perturbatively up to second order. In the second order energy shift term all angular momentum couplings of all hyperfine states with the chosen pair $|\uparrow\rangle\,,|\downarrow\rangle$ are summed up. To finally compute the potential, the dipole matrix elements arising

are reduced by the Wigner-Eckart Theorem to the familiar Clebsch-Gordon coefficients and a Wigner 6-j reduced matrix element. See [10, p.22-23] for a more detailed description. The potential calculated will be used for simulating lattice dynamics in chapter 4.

The potentials $U_\uparrow$ and $U_\downarrow$ can be shifted in relation to each other. This is accomplished by steering the phase of the circular polarisation components of the counterpropagating beam pair. During a potential transport step, atoms confined within will follow suit. This constitutes the way state dependent transport is realised in this setup.

Further details in how this position shift can be accomplished will be omitted here, referring to [7], [25], [42] for the two dimensional scheme and [8], [10], [51], [55] for the original one dimensional scheme as reference.

The ability to conduct state-dependent transport (shift operation) and change even for a single atom individually the polarisation state (coin operation) from $|\uparrow\rangle$ to $|\downarrow\rangle$ interchangeably by microwave pulses allows for the realisation of different kinds of discrete time quantum walks [11].

2.2   Cooling and trapping of atoms

In order to work with the atoms they have to be loaded into the lattice from the background vapour. In addition, cooling into the vibrational ground state of the lattice site in which the atom is confined is desireable. This enables the reproduction of indistinguishable atomic states. Those are required for probing quantum statistics [15]. It also allows for more reliable simulations and estimates of the dynamics due to knowing the precise initial state which will come to use in chapter 4.// The following section summarises the cooling and trapping mechanisms used in our experiment.

2.2.1   Magneto optical trap

Atoms have to be cooled to efficiently trap and compress them. This aspect will be revisited in 4.4.3. To cool a free atomic gas, all three independent directions have to be cooled simultaneously. This may be achieved to a degree with the optical Molasses technique. There six red detuned beams impinge on the atom. In case of atom movement towards a beam, the atoms are Doppler shifted into resonance to the beam and are subjected to an increased light scattering force counteracting their movement.

Trapping cooled atoms requires a spatially varying potential to confine them. This is accomplished by a MOT as seen in Fig.2.4 and was as a method first reported in [13].
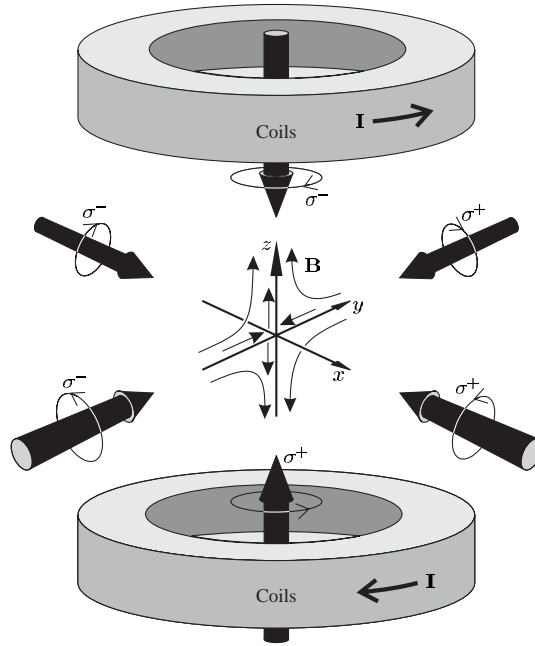
Figure 2.3: Magneto optical trap beam and magnetic field gradient configuration. The magnetic gradient induces a Zeeman shift creating a position dependent potential with minimum in the quadrupole field center which traps slow atoms. The counter-polarised beams are chosen such that their relative detuning to the cooling transition leads to an increased scattering force for atoms moving out of the center in all orientations , molasses cooling them thus. [56, p.192].

Due to off-resonant scattering, an additional repump beam is required to pump from the dark $6^2S_{\frac{1}{2}}$ F = 3 state to $6^2P_{\frac{3}{2}}$, F =4 in order to decay back into the cooling cycle.
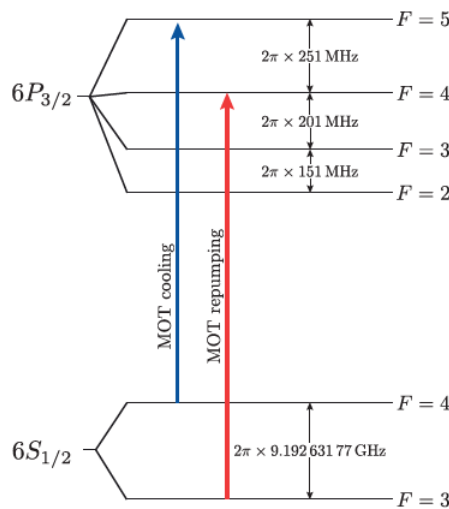
Figure 2.4: Cooling and repumping cycle for the MOT [8, p.7].

To load the atoms into the HDT, the center of the MOT is shifted upwards by adding a magnetic offset using the the compensation coils such that the MOT

then overlaps with the HDT lattice. See Fig.2.5 for the schematic setup of the coil geometry.
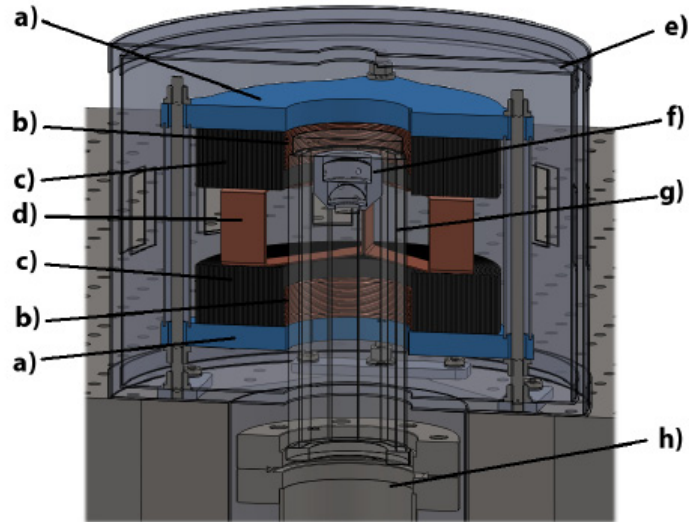
Figure 2.5: Experimental area: a) water cooled plates, b) z-compensation coils, c) z-gradient aluminium band coils, d) x=y-compensation coils, e) double-layer μ-metal shielding against high frequent magnetic fields, f) high NA-objective (NA = 0.92) [17], g) twelve-sided vacuum glass cell [7], h) connection to vacuum maintaining. Taken from [42, p.16] The compensation coils not only are counteracting stray magnetic fields. They also provide the quantisation axis along the counterpropagating beams.

After overlapping the MOT with the HDT lattice, the loading of the thus cooled atoms into the lattice becomes possible following [70, p.52].
The atoms are then confined within single lattice sites with their motional state given by the respective lattice site's vibrational levels they occupy.
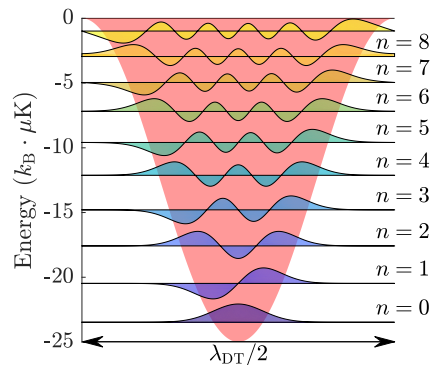
Figure 2.6: Vibrational level structure of a single lattice site of a sinusoidal potential [55, p.27].

2.2.2   Three dimensional ground state cooling

To reach the vibrational ground state sub-Doppler cooling is required.
In our applications it is preferred to avoid the atomic losses experienced by other

standard cooling methods like evaporative cooling with which reaching a Bose-Einstein Condensate was accomplished[16]. The technique used in our experiment is so called sideband cooling. Depending on the direction to be cooled, either Raman or Microwave sideband cooling comes to use in our setup [8].

Raman sideband cooling First, an overview will be given about the Raman sideband cooling method for free atoms and then the application in the cooling to the vibrational ground state will be further explored.

The Raman two photon process is distinctively different from the common single photon transitions. Two Raman photons coherently drive an atom over an intermediate virtual level to an excited state. Both transitions are with negligible spontaneous losses. Concerning cooling a free atomic ensemble, the advantage of Raman driven cooling is the higher sensitivity to Doppler shifting than in the single photon case [56, p.209]. This higher sensitivity is exploited in the scheme presented in Fig. 2.7.
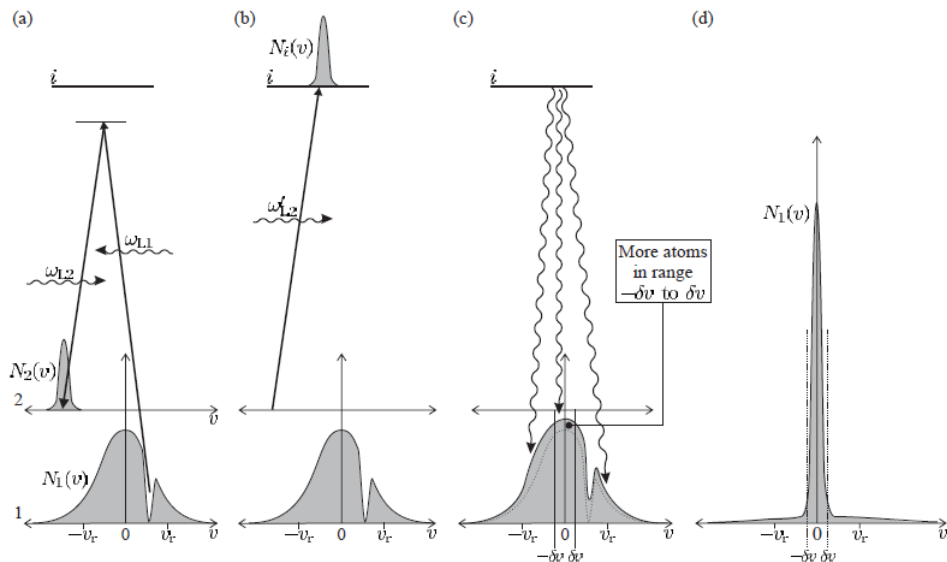
Figure 2.7: a) Two counterpropagating laser beams are on frequencies far from resonance to the state 1-2 gap. Their difference frequency though is close to resonance to the 1-2 transition. Atoms in a very narrow velocity distribution have velocities such as to be on resonance to 1-2 when adding the laser difference frequency to the Doppler shift. Those atoms are thus by a Raman two photon process mediated over a virtual level excited from 1 to 2. Let the starting mean velocity of the atomic ensemble before excitation be v. When on level 2 they will have experienced two recoils from Raman photons, leading to mean velocity $v - 2v_r$ with v_r the velocity change due to emitting a Raman photon. b) A third beam excites the atom to a higher level in which they will have a mean velocity of about $v - v_r$. c) Then they may spontaneously decay to a mean velocity between v and $v - 2v_r$ back to level 1. After this last transition the number of atoms with v around 0 increases. d) After numerous iterations while scanning the Raman beam detuning the final velocity distribution will be sharper and centred around 0 with a distribution width given by the sensitivity of the Raman process [56, p.211].

In our experiment, state 1 and 2 are the $|\uparrow\rangle$ and $|\downarrow\rangle$ states from before on the same vertical dipole trap (VDT) lattice site. Two Raman beams along the

vertical lattice direction are here detuned such that instead of being selective to a certain velocity range they are selective to a vibrational transition of the dipole trap. Transferring from some vibrational level n ,$|\uparrow, n\rangle$ to the same n, $|\downarrow, n\rangle$ is called a carrier transition while detuning leads to sideband transitions $|\uparrow, n\rangle$ to $|\downarrow, n \pm 1\rangle$. To actually cool the atom to a vibrational level lower than the initial starting state, the MOT repumper beam is used. Here off-resonant excitations of the atom and spontaneous decay back into the $|\uparrow\rangle$ is functioning as the third beam from Fig. 2.7.

Microwave sideband cooling   It is more convenient to employ microwave coupling between different vibrational states for cooling along the horizontal directions. The problem that a single microwave photon cannot give a large enough momentum kick to allow for vibrational transition [8, p.53-54] can be circumvented. The procedure is as follows:

Along the direction where atoms can be state-dependently transported, one first applies a microwave transition in resonance with the $|\uparrow, n\rangle$ to $|\downarrow, n-1\rangle$ transition. If performed while moving the $|\uparrow\rangle$ and $|\downarrow\rangle$ potentials over a certain distance Δx, this allows for similar coupling strengths as in the Raman sideband cooling case between vibrational levels for different sites.
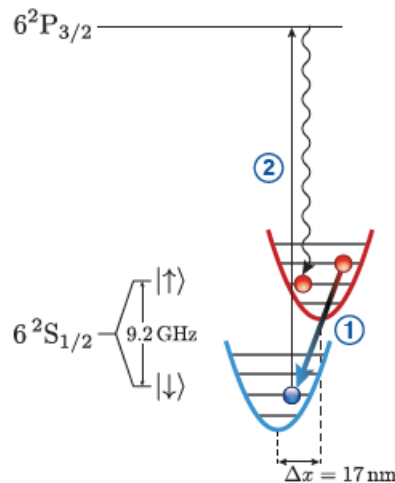
Figure 2.8: Microwave sideband cooling procedure. 1 being the resonant transition driven to lower the vibrational quantum number, 2 the off-resonant scattering transition [8, p.54].

With Microwave sideband cooling it is thus possible to cool along the HDT-plane directions and with Raman cooling orthogonal to it along the vertical direction.

With atoms cooled to the vibrational ground state of our trap, experimental sequences may be employed. Their outcome would be monitored then by observing the fluorescence arising from excitations due to the molasses beams of the MOT. This fluorescence may be picked up employing the high NA objective in combination with the VDT confinement.

2.3 Limitations of the experimental setup

After having discussed the experimental routine, the limitations will be reviewed with special emphasis on the points addressed by the rest of this thesis.

2.3.1 Limitations due to vertical dipole trap

Employing the vertical dipole trap is necessary for 3D ground state cooling into its vibrational ground state with the Raman sideband method. It also allows in principle single site detection by setting the conditions in which the full NA of the objective may be used. But it also has at present major drawbacks. The reason becomes apparent observing Fig. 2.9.
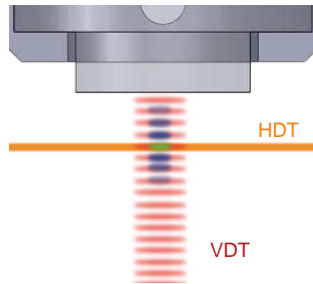
Figure 2.9: On site view of the beam configuration of Fig. 2.2a. Additional planes of the VDT (red) are populated besides the target plane encompassing the HDT (yellow).

Atoms can be trapped out-of-focus within the vertical dipole trap while overlapping lattice and MOT. In the current setup observation of the vertical axis is not yet accomplished. Therefore the trapped atoms are unknown distances away from the center plane. In order to conduct interacting quantum walks atoms [6], single plane occupation only is required. In addition, the imaging suffers twofold by the presence of the out-of-focus atoms. First they decrease the atom detection efficiency due to providing additional background light. Second they also create aberrations that make themselves apparent by blurred peaks or intensity rings[7, p.51].

From the one dimensional realisation of the DQSIM setup a method is already in use to achieve single site occupation [18, pp.5-6]. The same method could be applied in the present case to achieve single plane occupancy. The idea is to apply a magnetic gradient field and a constant offset field along the vertical axis. Due to the Zeeman effect the transition frequency between $|\uparrow\rangle$ and $|\downarrow\rangle$ resonances will be shifted the following way[18, p.5] :

$$\delta\omega = \gamma B_0 + \gamma\nabla(B)z + r^2\frac{\gamma\nabla(B)^2}{8B_0} \qquad , \qquad (2.2)$$

where B_0 denotes the constant compensation field, γ the hyperfine gyromagnetic ratio of 2π 2.5 MHz/G, z the coordinate along the vertical lattice and r the radial distance along the HDT planes from the center of the coils.

Initialising all atoms in the $|\uparrow\rangle$ state can be achieved by optical pumping. This is followed by applying a π- microwave pulse. It has to be narrow enough in frequency to only address in a single plane the transition from $|\uparrow\rangle$ to $|\downarrow\rangle$. A resonant push out beam[37] may eliminates all atoms still in the $|\uparrow\rangle$ state. The very same atoms in

different planes. In the one dimensional setup employing a rectangular microwave pulse for example leads to a sinc-occupation distribution after homogeneous filling of sites :
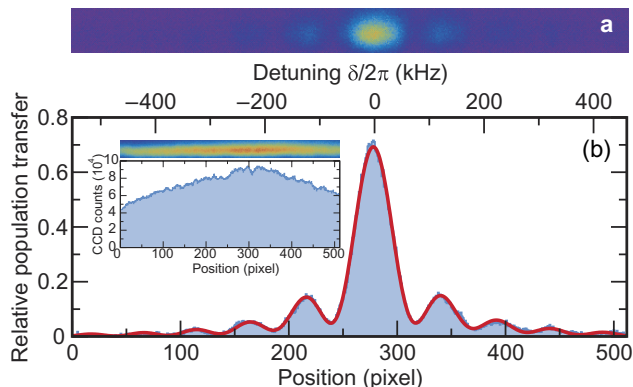
Figure 2.10: Applying by a magnetic gradient a position dependent Zeeman shift in the transition frequency allowed pushing out atoms of undesired lattice sites in [18].

In our case we may use the gradient coils to generate the gradient field and rotate the compensation coil field along the vertical axis to have a controllable B_0 offset to target the plane.

This thesis addresses two challenges that still are required before plane selection is feasible. It is desirable to have as many atoms as possible in the target plane and in the vicinity of the coil axis center. The reason for the latter is the radial dependency of the frequency shift in equation 2.2. From it follows that even atoms in the target plane may remain in $|\uparrow\rangle$ in large radial distances. To estimate the severity of this limitation:

Assume first a gradient field of $\gamma\nabla(B)/(2\pi) = 40$ kHz frequency detuning per vertical lattice site. Driving the maximal current through our gradient coils, such a gradient field is realistic for our setup [7, p.56]. Concerning the constant guiding field, we assume a strength in the order of about 1 Gauss, similar in strength to the field strength used for defining the quantisation axis [7, p.56]. The detuning of atoms about 16 horizontal lattice sites away from the coil axis center is then the same as for atoms in an undesired different plane. Such atoms would then be lost during a state-selective push after performing a microwave pulse driven transition even though they are in the desired target plane. The atomic spread can be estimated to be in the order of the 1/e-width of 50 μm of the MOT overlapping with the lattice. This translates to more than 100 lattice sites .

A different way for reducing the limitation arising from the radial dependency of the detuning would be increasing the guiding field strength. This would extend the radial region within which atoms may be addressed by a microwave pulse selectively. Then driving current noise would at some point limit the selectivity of the plane selection while compression along the horizontal directions comes with no such drawback. So a compression in the horizontal plane of at least 16 lattice sites is aimed at. For the compression along the vertical direction a single plane would be optimal to reduce the atom loss experienced by the state-selective push-out beam. Those compression schemes will be discussed in detail in chapter 4.

The second challenge can be illustrated from the microwave Gaussian pulse used to address the target plane. A frequency width of $\Delta\nu = 20$ kHz translates into a

temporal duration $\Delta t = \frac{4\log(2)}{\Delta\nu} \approx 140\,\mu s$. In order for atoms to remain stable during this time in the initialised state, decoherence and heating mechanisms have to be addressed. And one aspect as it will turn out, is going to be dealing with a stable laser intensity which may be improved following chapter 3.

2.3.2   Decoherence and heating mechanisms

The experimental procedure is limited in time by either heating or decoherence effects. Heating refers to the process of losing the atom due to interaction. Those interactions increase the atom's kinetic energy enough to escape the lattice altogether.

Decoherence also refers to interactions with the uncontrolled environment. But those do not necessarily lead to a loss of the atom in the lattice but to loss of stability in maintaining their initialised state without any coin operations applied. In this context of an effective two level system of $|\uparrow\rangle$ and $|\downarrow\rangle$ a simplified model may be introduced by the

   -Sphere picture to describe decoherence.

There the dynamics of a two level atom interacting with an electric field may be described by the optical Bloch equations. By Introducing two additional loss time constants, decoherence may be added[10, p.34].

$$
\begin{aligned}
\dot{u} &= -\delta v + \Omega_R w - \frac{u}{T_t} \\
\dot{v} &= \delta u - \frac{v}{T_t} \\
\dot{w} &= -\Omega_R u - \frac{w - w(t=0)}{T_1}
\end{aligned}
\qquad , \quad (2.3)
$$

with δ the detuning, Ω_R the Rabi frequency, T_t the transverse, T_l the longitudinal coherence time, w the population inversion and u twice the real part and v twice the imaginary part of the off-diagonal element of the density matrix of the two level system.

Longitudinal decoherence leads to a rate of spontaneous decay of the initialised state. This includes also transition outside of the the two level system. Because of the long lifetime of the Cs-hyperfine states, relevant transitions out of the two level system occur usually due to scattering events [10, p.40]. In contrast the loss of phase relations between the two states in case of a superposition is determined by transverse decoherence loss terms [19, p.266]. This can be visualised by assuming a superposition state of the two levels initially. This state lies thus on the u-axis in the equator of the sphere. The transversal decoherence leads to a precession movement around the w-axis of the (u,v,w)- Bloch vector, Fig. 2.11.
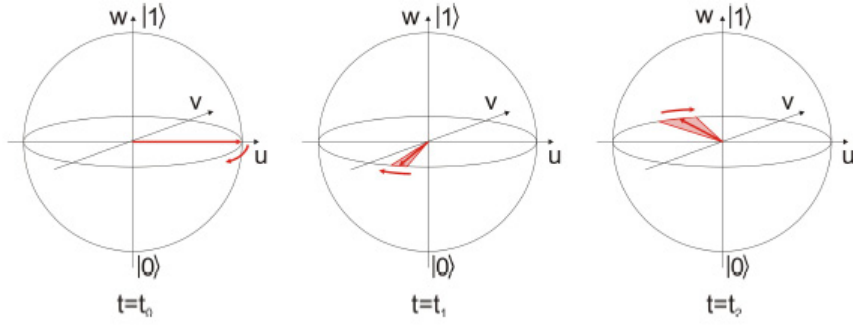
Figure 2.11: Precession movement in the Bloch sphere equator region due to transverse decoherence on $\frac{1}{\sqrt{2}}(|\downarrow\rangle + |\uparrow\rangle)$ in a two level system [10, p.35].

This in turn leads to an imperfect transfer of population to the $w = 1$ state after applying a $\int_0^T \Omega_R(t)\mathrm{d}t = \frac{\pi}{2}$ pulse.
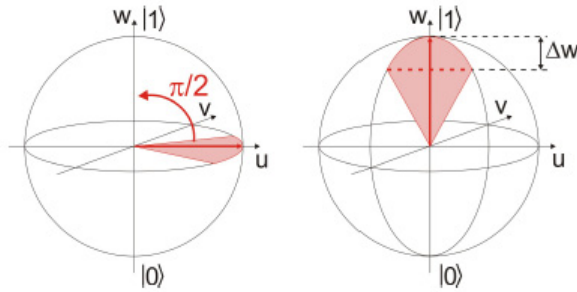
Figure 2.12: Incomplete population transfer after applying a $\frac{\pi}{2}$ pulse on the previous superposition state [10, p.36].

Inhomogeneous transversal decoherence within an atomic ensemble may be compensated by employing spin echo [54]. But non-differential decoherence in the long term time can only be reduced by removing the causes from which it stems .

A short list of heating and decoherence mechanisms will conclude this chapter:

1. Pointing instability   Pointing instabilities refer to any sort of change in the beam's orientation in form of angular or parallel displacement. This could arise from changes the alignment optics may experience coming from air flows in the lab, temperature changes leading to deformation or mechanical vibration on the optical table and alike. A change in the degree the beams overlap or cross would change the lattice geometry seen in Fig. 2.2b. Fluctuations thereof translate in a jitter of the lattice constant, potential maxima, minima shapes and the transport direction. Using a quadrature photodiode sensors like the PDQ80 [57] allows monitoring and debugging pointing instabilities and is in the process of being installed in the DQSIM experiment.

2. Phase noise   Because the polarisation of the HDT1,3 beams is employed to shift the lattice potential for either atomic polarisation state, differential noise in the polarisation purity would lead to jittering of the potential positions. This turned out

15

to be a major source of heating [21] and decoherence [22] in our setup. Based on that extensive studies in optimising the polarisation synthesis and stability with phase locked loops were accomplised in our group (see for example [60] [25]). Common mode phase noise may imprint an inertial force on the atoms subjecting the atoms to a phase gradient. This in turn reduces their coherence during transport [22, p.26].

3. Magnetic field fluctuations   Magnetic field fluctuations change the Zeeman-shift of the hyperfine state. This leads to fluctuations of the detuning and therefore of the dipole potential shape and depth causing heating and decoherence similarly to pointing instabilities [10, p.39]. A current stealing circuitry to stabilise the coil driving currents for our compensation coils is employed to minimise effects like this. And additional adjustment for the gradient coils is currently being developed which is of necessity to accomplish plane selection.

4. Scattering with the background atomic vapour   The absolute lifetime of the atoms in the optical lattice is in the best case limited by scattering with the background vapour in the order of tens of seconds .
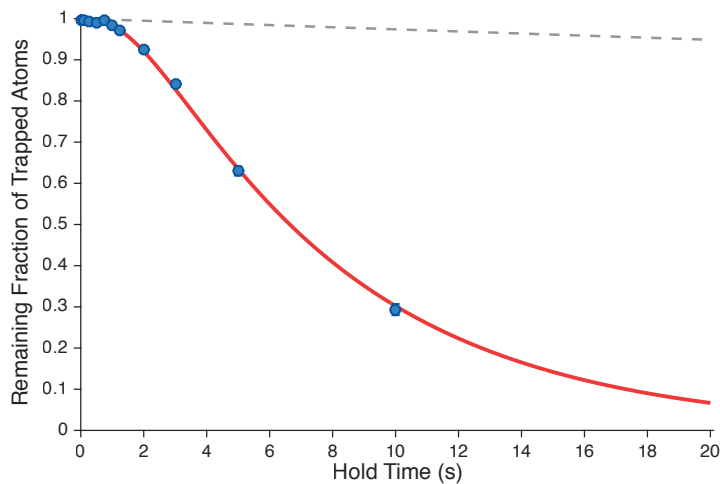
Figure 2.13: Measured storage time of the atoms (blue points), simulation by Focker planck equation following [59] (red line) and the life time limit arising from background scattering alone (grey dashed line) in the one dimensional setup [8, p.11].

5. Light scattering   Any light scattering is going to be detrimental to a quantum walk. Recoil heating due to spontaneous emission will always be present. Scattering with light may be in principle elastic or inelastic too.
Elastic scattering such as Rayleigh scattering is going to induce spin dephasing while Raman scattering in addition will mix the populations [22, p.27]. Those scattering effects are the reason for transitioning to a shallow lattice for experimentation and a deep lattice for trapping and imaging by applying an adiabatic ramp to the HDT beam powers[8, p.10].

6. Beam power mismatch   Different beam strengths would lead to a more complicated make up of the potential according to equation 2.1 as the intensity pattern

would differ . This causes different trap depths, lattice constants combining in a sense the effect of phase noise and intensity noise when the mismatch is fluctuating.

7. Potential crosstalk and transport phase ramp shape Performing a transport step will lead depending on the phase ramp shape to atoms not staying in the initial vibrational state of the trap.

In addition during transport the specific shape of the potential affects the transport quality too. The potential for the $|\uparrow\rangle$ is only dependent on the σ^+ light polarisation spatial interference pattern while the $|\downarrow\rangle$ shows a crosstalk between the two circular polarisations. This leads to an amplitude modulation of the potential depth during a transport step. This additionally produces for the latter species decoherence and heating. Both effects can be reduced by shaping the ramp to compensate for this effect via optimal control [51][55].

8. Differential light shifts from populating multiple vibrational states
If an atom populates multiple vibrational levels it will experience a different detuning depending on its concrete distribution over the vibrational levels leading to dephasing [22, p.22]. This would be remedied by three dimensional ground state cooling.

9. Inhomogeneities of the potential due to the laser beam profile The finite width of the laser beams will lead to a flattening of the potential depth the further from the center one operates. This decrease in depth will translate in an increase in hopping rates [61, p.47]. Also, atoms will experience a different vibrational level structure due to the flattening of the potential at the edge . Similarly, they will not be efficiently addressed by a single microwave pulses due to changing Zeeman shifts over certain distances as seen in 2.3.1. Compression along the vertical direction will allow avoiding such inhomogeneities to play a dominant role.

10. Intensity fluctuations Intensity fluctuations translate directly into changes of the dipole potential depth making up the optical lattice as can be seen from equation 2.1 and may arise from multiple sources. For example it may come from intrinsic noise of the power supplies or electromagnetic interference (EMI) coupling into any sort of electronic driving the beam intensity. This would apply to noise at frequencies capable of modulating the amplitude of the RF-signal driving an Acusto-Optical-Modulator or electro optical modulator. Pointing instabilities themselves may translate into varying coupling efficiencies thus fluctuating out-coupled beam power in the case of optical fibers or tapered amplifiers for example. Or fluctuations originate internally from the way the gain medium of the laser is driven by current noise for laser diodes or tapered amplifiers, relaxation oscillations in the gain medium itself or cavity losses. The effect intensity fluctuations have on heating is (in first order perturbation theory using a harmonic approximation of the lattice potential) [21, p.56]:

$$\langle \dot{E} \rangle = \frac{\pi}{2} \omega_{\text{tr}}^2 \langle E \rangle S_\epsilon(2\omega_{\text{tr}}) \qquad , \tag{2.4}$$

with $\langle \dot{E} \rangle$ the rate of change in the energy of the atom, ω_{tr} the trapping frequency which is proportional to the square root of the trap depth in the harmonic approximation and $S_\epsilon(2\omega_{\text{tr}})$ the one sided power spectrum of the relative intensity fluctuations

$\epsilon(t)$. The limitations intensity noise causes on decoherence is [22, p.24]:

$$p_c = 1 - \exp(-\Delta\Phi^2/2) \approx \Delta\Phi^2/2$$
$$= \frac{\tau^2\eta^2 U_0^2}{2\hbar^2} \int_0^\infty \mathrm{sinc}^2(\omega\tau/2)\mathrm{RIN}(\omega)d\omega, \tag{2.5}$$

with $1 - p_c$ is the decay term of the off-diagonal density matrix elements. It is related to the time evolution of the u and v component of the Bloch vector per definition. Therefore $1 - p_c$ provides in the Bloch sphere picture the time scale for decoherence driven precession movements of the Bloch vector around the w - axis as mentioned in 2.3.2. RIN describes the relative intensity noise and means normalising fluctuations in the sense of signal to noise ratio by the laser beam power. Equation 2.5 reveals that decoherence arising from intensity fluctuations is mainly contributed by lower frequency noise in the order of magnitude of $1/\tau$, with τ being the duration of a single step of the quantum walk. In our case τ is typically in the order of $20\,\mu s$ [78, p.9774] and therefore noise up to $100\,\mathrm{kHz}$ is of special importance to be suppressed.

2.4   Measuring decoherence

As a brief outline concerning how to measure the T_1 and T_l times as quantities characterising the decoherence effects acting on the system : The population relaxation can be simply measured by a state-dependent detection for different holding times [8, p.41] while the dephasing can be measured by contrast measurements of an atomic interferometer [63].

To summarise this chapter: This thesis is going to focus on contributing to the reduction of the effects of intensity fluctuations by overcoming the current limitations of our lattice beam intensity stabilisation setup.
The compression scheme may be used to avoid limitations due to inhomogeneities in order to improve the experimental setup further in its coherence time and performance and to contribute in achieving plane selection.

3 INTENSITY STABILISATION

This chapter introduces the intensity stabilisation setup of the DQSIM experiment and how a new photodiode amplifier circuit may improve the noise suppression. It starts with sketching the setup. Then the current limitations will be inferred and explained and based on those assessments a new design for a sensor photodiode (PD) motivated. Its circuitry will then be reviewed and characterisations briefly summarised. Then this chapter concludes with a test setup intensity stabilisation result.

3.1 Laser intensity stabilisation setup

The intensity stabilisation in the DQSIM experiment consists of an analog and a digital control system in series. This combines the high bandwidth of the analog intensity stabilisation with the flexibility of programming scripts for fast intensity modulation provided by digital control. The analog control box[1] and stabilisation as well as the Keysight module and digital stabilisation is implemented and described in [26].
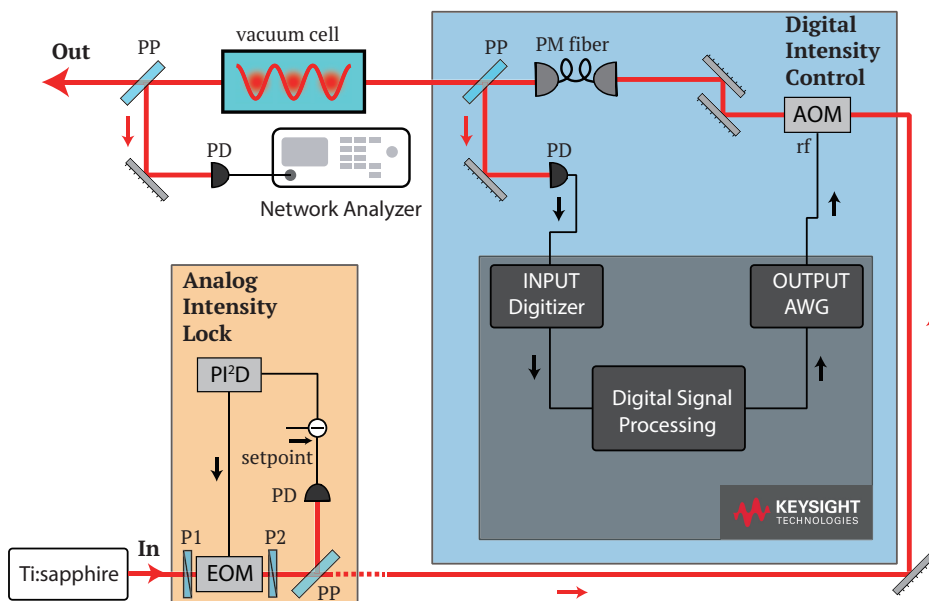
Figure 3.1: Block diagram of entire intensity control system. The part with an orange background is the analog intensity lock, and the part with a blue background is the digital intensity control system. Abbreviations: P1,P2: polarizer, EOM: electro-optic modulator, PD: photodiode, PP: pickup plate, rf: radio frequency, PI^{2}D : proportional-double-integral-derivative controller, AOM: acousto-optic modulator, AWG: arbitrary waveform generator [26, p.5].

The digital block starts first with coupling the beam into an acousto-optic modulator (AOM).

---

[1]Vescent Control Box D2-125

Its zeroth order is then dumped and the first order is coupled into a fiber and from there split by a pick-up plate. The beam either goes to the atoms or hitting the monitoring photodiode[2] (TPD) at the moment. Its output is sent to the input of the Keysight module where it is digitized. The desired DC value is then subtracted and the FPGA (field programmable gate array) programming is employed to apply PID control on the error signal. This error signal is going to modulate at 80 MHz carrier frequency the Keysight module's arbitrary waveform generator output. This output is fed, after going through a RF amplifier, into the RF signal input of the AOM to modulate and stabilise the first order appropriately.

3.2   Function of the AOM

The AOM will be used in the test setup to imprint additional noise on the beam to quantify the suppression achieved by the new photodiode. How this may be accomplished will be discussed in the following section.

3.2.1   Principles of AOM operation

An AOM is serving as the actuator device able to electronically steer the angle, amplitude and frequency of a beam based on the RF-signal it receives.

---

[2]Thorlabs PDA-10EC
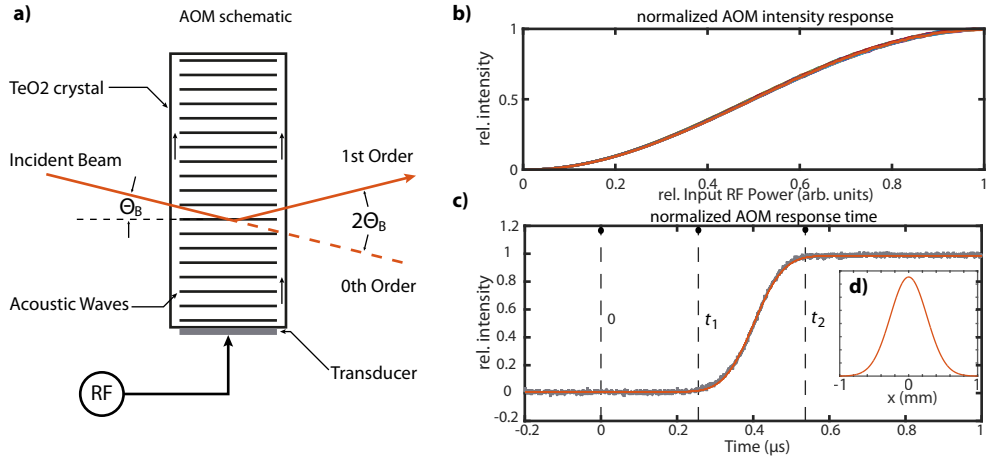
Figure 3.2: a) Schematic drawing of the AOM and the beam path propagation. The Bragg-angle between the incident beam and the moving diffraction grating in the AOM-crystal is given by Θ_B. RF is short for the radio frequency source of the transducer. b) Relative intensity response of the AOM to a signals of different powers. The figure depicts an average of multiple measurements, normalized to the corresponding maximum intensity. This ensures the independence from laser intensity drifts. c) AOM step response versus time. The radio signal is switched on instantly at t = 0 (blue), and the output of the AOM is measured with a fast photo diode (red). The dead time of the AOM is indicated by t_1, whereas t_2 denotes the time until the steady state value of of the intensity is reached (rise time). The data is fitted with an error function (red). d) Gaussian beam profile calculated from the fitted error function. From [25, p.10].

The RF signal drives the transducer to vibrate, generating sound waves contracting and expanding the density of the transducer material. This translates into variation of the refraction index periodically. This pattern of changing refraction indices acts on the beam as a Bragg lattice generating a first order diffracted beam. By modulating the RF signal the changes on the effective lattice will translate in modulation of amplitude, angle and frequency of the first diffracted order beam, see Fig.3.2.

3.2.2 Usage in setup and test setup

The AOM can be employed in the intensity stabilisation to modulate the first diffracted order accordingly. The lattice beams and thus the potential may be stabilised by the PID control tuning the RF signal. With this procedure the noise of the first order can be reduced. The AOM rising time limits the bandwidth with which it can follow the RF signal. The rising time depends on the beam diameter as the rising time follows from the speed of sound inside the AOM crystal over the full width of the coupled-in beam. For the AOM used [3] the rising time does not limit the control bandwidth in a substantial way if properly focused (25 ns rising time or above 10 MHz).

The steeper the slope of its diffraction efficiency happens to be for the operating RF amplitude, the more sensitive the beam modulation is to RF amplitude modulation.

---

[3] AOMO 3080-125

21

Sensitivity to noise coupling in and imprinting on the beam is also enhanced in this regime. This will be used to increase the noise floor artificially in the test setup by adding from a noise generator an additional signal to the photodiode output.

3.3 Current intensity stabilisation limitations

The limitation of the current setup arises from read-out noise[26]. In the following, the effect of read-out noise will be elaborated. The measured noise traces of the current setup are then discussed and the conclusions drawn from it presented which are going to motivate the new photodiode design.

3.3.1 Read-out noise

Noise arising from the system, setpoint, the feedback path or the controller input would experience different transfer functions depending on where they are injected. Intuitively in the best case coupled in noise would be similarly suppressed as signal noise. But this would still lead to unsatisfactory suppression of noise of other origins than the laser. This is because the PID parameter are optimised for the laser noise input path. Moreover any transfer function is only going to be able to attenuate noise at a certain frequency by a finite factor. Any additional noise source will degrade the noise floor of the stabilised laser.

From the setup in Fig. 3.1 many different noise sources could couple to the original noisy laser signal. In the following we focus on the read-out noise of the Keysight module input [30].

If the coupled-in noise is sensor or read-out noise ($\epsilon(t)$), its presence counteracts noise suppression for signal noise. Compared to the intrinsic laser noise $d(t)$, sensor noise and read-out noise are indistinguishable from the reference input $r(t)$ leading to the following error signal in the output $y(t)$ following [52, p.789]:

$$R(s) - Y(s) = G(s)(R(s) - D(s)) + (1 - G(s))E(s) \tag{3.1}$$

with Laplace transform introduced in the appendix being $\mathcal{L}[r(t)] = R(s)$ etc., and $G(s)$ the suppression gain experienced due to feedback. One has to make a trade-off in optimising noise suppression and reducing sensor noise imprinting on the signal when dealing with sensor noise and read-out noise.

3.3.2 Noise in the current setup

The input port of the Keysight module can be adjusted to be a 50 Ohm input impedance to the source or $1\,\mathrm{M\Omega}$ (HiZ) input impedance and the voltage scale can be continuously adjusted between 0.4 V_{pp}, 50 Ω or 0.2 V_{pp}, HiZ to 6 V_{pp}, 50 Ω or $20\,V_{pp}$, HiZ. For the stability of the intensity locking we prefer to use the full dynamical range and a HiZ input impedance . Otherwise voltage spikes would drive the input close to the nonlinear regime where control theory cannot the effect of the control action.
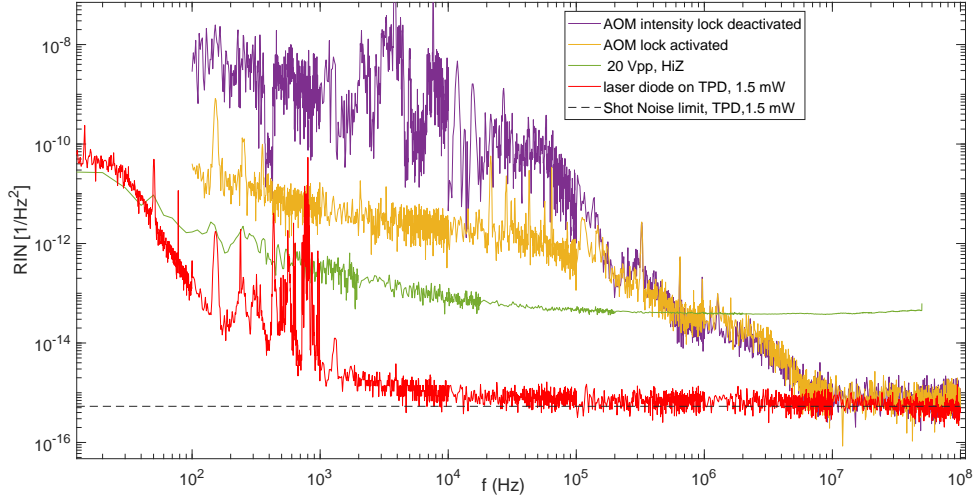
Figure 3.3: The violet trace corresponds to the Titanium Saphire (Tisa) laser intensity noise. It was measured out-of-loop and converted into units of RIN^2 with AOM intensity stabilisation disabled. The yellow trace is with active AOM stabilisation. In both cases the analogue lock was enabled. The green trace is the Keysight module input noise for HiZ input impedance and the full dynamical range of 20 V_{pp} in RIN relative to the output of the TPD. The red trace is the TPD measured laser noise of a laser diode being mostly shot noise limited.

In Fig. 3.3 the stabilised intensity noise is only slightly above the read-out noise in the preferred setting of the Keysight module. The lacking sensitivity due to this input noise is illustrated by the shot noise detected for a quiet laser source with the same TPD. The current monitoring photodiode isn't limiting us due to being shot noise limited itself. Nor is the limitation shot noise as the physical limit of non-squeezed intensity noise. That leaves the input noise of the digital control unit with a read-out noise two decades above the TPD shot noise limit.

There can be two origins for this high read-out noise: Either it is due to digital noise coming from the quantisation error of the module's digitizer. Or it originates from the internal analog electronics of the Keysight module before the digitizer which are necessary to adjust the input impedance and voltage range scaling. The traces of the read-out noise have been measured employing the DAQ command of the Keysight module's matlab[24] class for an input port terminated with $50\,\Omega$. The read-out data is then DC offset subtracted and Fourier transformed and averaged after calibrating it.

The two traces of the TiSa noise are measured out-of-loop by the TPD and are then after inserting a DC block spectrally analysed using a HP 3589A Network Analyzer (NWA) The relative intensity noise (RIN) for all traces is normalised by the input power measured by the TPD.

Two conclusions may be drawn from Fig. 3.3 which are of relevance to improving the current intensity stabilisation.

Read-out noise The difference between $50\,\Omega$ and HiZ is too large to arise from the input impedance alone. Due to the input impedance, voltage detection and therefore voltage noise should differ by a factor of 2 or 6 dB. The much larger noise

floor of nearly 30 decades therefore has to arise from internal electronics of the input settings or from the digitizer error[4].

The bandwidth of the digitizer is some 50 MHz [30]. If the noise would arise from digitising errors it would show limitations due to the digitizers own bandwidth. Therefore it is most likely noise arising from internal analog electronics. This loss in sensitivity can be translated into a reduction of the numbers of available bits from specified 16 bits to 10.4 bits in the worst case effectively [26]. Operating at the full dynamical range is desirable though as the setpoint subtraction happens inside the controller and the TPD output range for HiZ is 10 V at max. In addition nonlinear behaviour of the Keysight module was noticed for voltage inputs above roughly 7 V. So even far away from saturation of the TPD not using the full dynamical range is going to degrade the control performance considerably. For example a large enough spike entering the non-linear regime may lead to losing the lock.

PID parameters The crossing frequency between stabilised and unstabilised laser intensity noise is at some 200 kHz which is an indication of the closed-loop bandwidth of the intensity lock. Similarly to the treatment of the standard second order system in the appendix, usually the transfer function phase starts to approach a sign change during gain roll-off. Inverting the feedback sign leads there to gain peaking. In case of PID intensity noise suppression the sign change translates into enhancement instead of suppression of noise during roll-off, a so called servo bump. The servo-bump will then be cut off by the limited bandwidth at the crossing frequency [65, p.250]. The absence of the servo bump here may be indicative to read-out noise being close to the laser noise in the position of the servo bump.

In case of read-out noise limiting the stabilisation, allowing for increased lower noise suppression gain would lead to more enhancement not only of the servo-bump but also to the read-out noise, following equation 3.1. A high and rather white read-out noise spectrum like the one from the Keysight module therefore requires reducing lower noise suppression. As explained in the chapter 2.3, lower frequency noise is more detrimental to coherence than higher frequency noise. This means that improving the stabilisation by allowing better lower frequency suppression is going to benefit the coherence time of the atoms.

To conclude: The readout noise translates itself into an effective loss of resolution and hinders an effective noise suppression in the critical frequency range by a great amount. The next section introduces a possible remedy to this problem by replacing the TPD by a in-house-designed and constructed photodiode amplifier (PD).

3.4   Custom photodiode design

The custom designed photodiode should ideally have the following properties:

- A very low sensor noise error in its detection of intensity noise to avoid problems discussed before

- If it was able to low noise amplify the laser fluctuations thereby increasing the resolution of the digitizer effectively it would compensate the effect the Keysight module's input noise

---

[4]Controlled addition of noise to the signal would have possibly already reduced the loss in sensitivity had it been digitzing errors limiting the precision [52, p.823]

- The bandwidth has to be at least an order of magnitude higher than the closed-loop frequency response bandwidth [23] of the entire intensity stabilisation so in the order of above 1 MHz at least

- The picked up light for the intensity stabilisation is going to be in the order of around 1 mW where the PD should operate optimally

Those requirements can be accomplished by a standard transimpedance amplifier design and a differential amplifier in the second stage which will be shortly reviewed in the next section.

3.4.1 Circuit design

Using active components it has become common practice to divide the functions into multiple stages. The reason is that the requirement on a single stage would be difficult to fulfill by single transistor or operational amplifier (op amp) [48]. The input stage has to be sensitive with low signal-to-noise ratio even for higher bandwidths. The second stage has to amplify without too much added noise by enough to allow shot noise limitation above the Keysight input noise.

Transimpedance stage The input stage was chosen to be a transimpedance amplifier circuit(Fig.3.4) consisting of an op amp in negative feedback configuration.
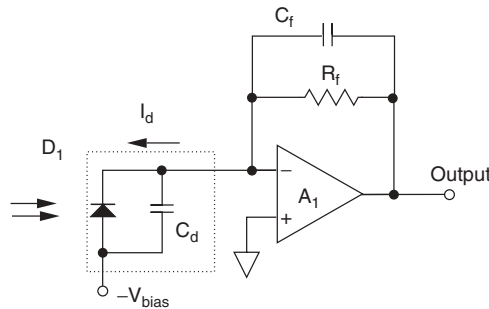

Figure 3.4: Transimpedance amplifier setup. The photosensitive chip is replace by a substitute circuit. D_1 the incident light power, C_d the photodiode capacitance, R_f the feedback resistor, C_f the feedback capacitor , I_d the photocurrent V_{bias} the reverse bias voltage, A_1 the operational amplifier [27, p.693].

In the following the function of each part will be explained starting with the operational amplifier or op amp: Op amp functionality following [17] can be summarised by describing an op amp as an integrated circuit with two inputs. It provides an open-loop voltage input gain to the voltage difference of its inputs of 10^5 to 10^6. For tuning their stability (and avoiding saturation), they are always employed in feedback configuration. An op amp has to compromise between speed and gain. This is usually specified in datasheets with the gain-bandwidth product or unity gain bandwidth.
The purpose of the op amp is to compensate for the photosensitive chip capacitance by tuning the feedback path which will become clear when discussing equation 3.3. Otherwise chip capacitance would severely limit the first stage bandwidth .
To introduce the open-loop transfer function of an op amp:

Modern op amps have usually an internal frequency compensation implemented. In the case of the so called dominant pole compensation the op amp is tailored by introducing an additional dominant lowest frequency pole. This additional lower frequency pole limits the bandwidth according to control theory.

This way unstable behaviour at higher frequencies is due to the bandwidth roll-off suppressed[27]. Freqency compensated op amps have an approximate open-loop transfer function of second order [27]:

$$A_{OL} = \frac{A_{DC}}{(1 + i\frac{f}{f_{\text{dom}}})(1 + i\frac{f}{f_2})} \quad , \tag{3.2}$$

with A_{DC} the DC voltage gain, f_{dom} the dominant pole frequency and f_2 the next highest internal system pole. Applying the op amp golden rules [17] and the results from the control theory recap one attains the transimpedance or effective resistance which the photocurrent will see [27] :

$$Z = \frac{Z_f A_{OL}}{1 + A_{OL} + i2\pi f Z_f C_d} \tag{3.3}$$

with feedback impedance $\frac{1}{Z_f} = \frac{1}{R_f} + 2\pi i f C_f$. Linearity is preserved up to the end of the bandwidth. The purpose of the resistor is just current-to-voltage conversion. The aim of introducing a feedback capacitor becomes clear from the transimpedance (3.3). The feedback capacitor similarly to a capacitance divider reduces the effects of the photodiode capacitance. Another point of view is its introduction of a dominant lower frequency pole just as in the frequency compensation case for op amps in general therefore reducing gain bandwidth and gain peaking by damping the system.

In order to use the full dynamical range of the Keysight module input, the non-inverting input of the op amp will be set to -9 V. This offsets the output by this amount enabling an output ±10 Volt. The choice of the feedback is motivated by allowing the op amp to operate at 0 Volt when the target laser impinges on the photosensitive chip. This may avoid additional issues arising from having to provide continuously a large voltage like heating. Knowing the chip, chosen to be a BPW34 peaking at the target wavelength of 866 nm in its responsivity, a $R_f = 15$ kΩ resistor was chosen. This would lead to a voltage output of zero after subtracting the offset for about $1\,\text{mW}$ incident power at 866 nm.

Voltage amplifier stage The second stage is a differential amplifier circuit(Fig.3.5) . Its feedback path can be similarly adjusted by a parallel feedback capacitor to improve stability if necessary. The DC value to subtract (to amplify only the fluctuations and avoid saturation in the second stage) can be provided externally or by a tunable internal voltage reference.
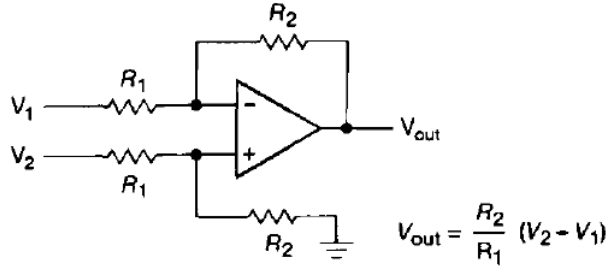
Figure 3.5: Difference amplifier schematic [17].

Its gain factor will be motivated in the next section after reviewing the sensor noise sources of the PD. The layout and schematics of the entire circuitry are in appendix D.

3.4.2 Internal noise and component choice

Assuming high quality resistors and a well isolated environment [5] with well filtered power supply rails, internal noise will limit the performance of the PD. Therefore a proper component choice has be made for which a short review of noise sources and limits will be conducted.

Possible laser noise origins and forms have already been discussed in chapter 2.3. The fundamental limit of laser noise arises from the photon statistics. In the following we assume non-squeezed states of light. The conversion of a photon to an electron introduces the counting variance of Poissonian statistics for this process. Even in the case of a limited quantum efficiency [28, p.384] it would translate to rms fluctuations of photocurrent I_d following the Schottky formula, so $\langle i_{\mathrm{shot}}^2 \rangle = 2eI_d$ with e the electron charge.

An additional noise limit, this time for resistors, is provided by noise arising from the fluctuation-dissipation theorem [49]. This leads to current fluctuations of $\langle i_{\mathrm{thermal}}^2 \rangle = 4k_b T/R$ with T the temperature of the resistor R.

Both shot and thermal or Johnson noise are white in the frequency domain.

The noise floor provided by the first stage has to originate for the target intensity from shot noise instead of being degraded by a bad resistor choice and becoming temperature dependent. For $15\,\mathrm{k\Omega}$ at $1\,\mathrm{mW}$ incident power and room temperature shot noise is going to be more than a factor of 6 larger than the Johnson noise contribution of the feedback resistor.

An important point to consider in addition, is noise arising from the op amp. The input current and voltage noise depends on the internal transistor setup making up the op amp. Usually a bipolar op amp has larger current noise and less voltage noise than a corresponding field effect transistor type, for more details see [48].

The current noise will see the same transfer function as the signal noise, similar to Johnson noise and shot noise, therefore degrading over all frequencies the signal to noise ratio. The voltage noise, v_{noise}, generates by coupling through the input capacitance of the op amp, C_{opamp}, an equivalent noise current [27] $\sqrt{\langle i^2 \rangle} = 2\pi f(C_d + C_{\mathrm{opamp}})v_{\mathrm{noise}}$. For higher frequencies the output voltage noise will increase due to this before being suppressed by the bandwidth limitation arising from the feedback capacitor, resulting in a servo bump.

The chosen op amp for both stages is the FET type AD8065 op amp. Its especially

---

[5]If not see appendix B

low current noise in the range of $pA/\sqrt{Hz}$ current input noise and voltage noise of the order of $nV/\sqrt{Hz}$ ensure a very low internal noise floor.

In addition for op amps, a high slew rate determines the speed at which the output can follow the input depending on the size it has to provide. Therefore this constitutes a measure for the small signal regime in which linearity holds. Ad8065's high slew rate allows even for steep small signal spikes to be treated linearly. This should improve the stability of the final intensity lock. Concerning its high bandwidth of 145 MHz, this allows for even higher compensation capacitance to reduce the detrimental effect of the photosensor capacitance while maintaining a high closed-loop bandwidth.

The second stage is aimed at providing an amplification big enough that shot noise overcomes the Keysight's module input noise and leading therefore to a negligible sensor noise effect. An amplification of a factor of 20 proved sufficient and allows still to maintain an overall bandwidth of above a MHz.

As can be seen in Fig. 3.6 the new photodiode has shown a well understood noise floor matching the datasheet specifications of all components and the expected noise contributions discussed. The shot noise limited light source at 1 mW was a diode laser (852 nm). To ensure the low additional noise which they are known to exhibit, single mode operation was observed with a small, portable Fabry-Perot cavity which our group developed.
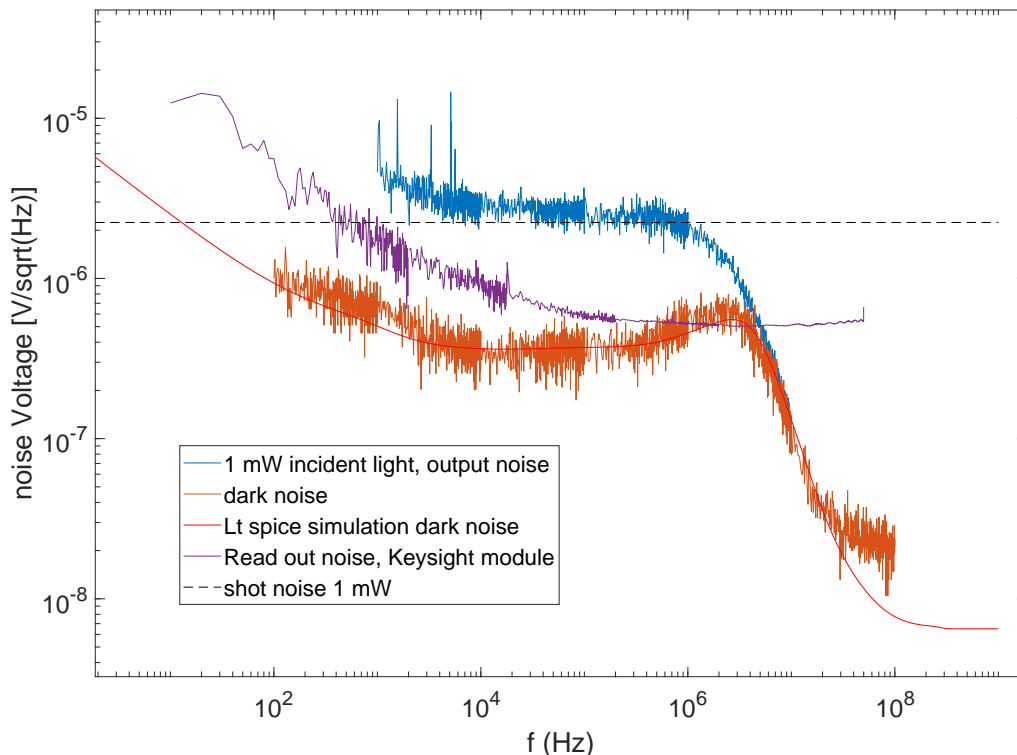
Figure 3.6: Keysight module input noise, output of the second stage of the custom made PD with and without incident power with 20 amplification gain of the first stage output and LTSpice simulation of the noise floor. The illuminated trace was taken by the NWA after shining on the Pd single mode laser diode light. The dark trace was measured in an entirely darkened room to avoid 50 Hz ceiling light noise. The DC voltage subtraction for the second stage comes from the internal, tunable voltage reference of the PD.

The dynamical range of the custom PD is not limited by this amplification as in principle the voltage compensation can be externally adjusted to by its AMP 03[77] differential amplifier input for an external setpoint setting.

The dynamical range given by the first stage amplifier, feedback resistor and photodiode chip is up to 2.4 mW input incident power.
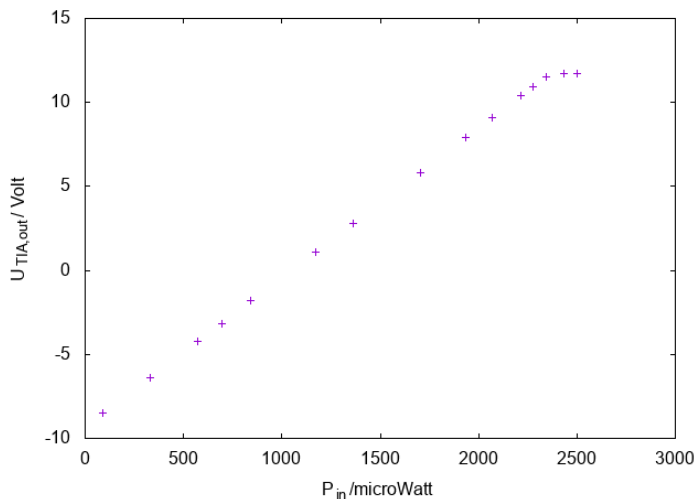

Figure 3.7: Output Voltage first stage transimpedance amplifier for AD8065 op amp and 15 kOhm feedback resistor, BPW 34 photodiode chip in dependency of the input incident power (852 nm).

3.4.3 Charge zone screening of photodiode chip

One note needs to be taken concerning the photosensitive chip. It requires a large reverse voltage applied to not degrade the speed of the first stage when higher powers in the sense of Fig. 3.7 are illuminating it. This is due to the charge zone effect within its depletion zone and will be in the following more elaborated.

Photodiode chip Light detection is usually performed employing the photoelectric effect occurring in a semiconductor's pn junction leading to the name photodiode. The following summarises the properties following [31, chapter 1].
The junction arises from combining different doping regions thus creating a depletion region generated by hole-electron recombination driven by diffusion.
The charge imbalance then leads to the formation of an electric field counteracting the diffusion current in equilibrium. Applying an external electric field in reverse to the junction leads to an increase of the depletion region size. The effective capacitance in this diode is then reduced. The photoeffect ensures linearity between photocurrent and input light power below saturation. The semiconductor material band gap determines what photon wavelength is required to allow for electron transitions to the conduction band. Silicon's band structure allows for sensitivity to infrared radiation (IR).
Adding an intrinsic layer in addition in between thogse two differently doped regions leads to the PIN photodiode design in Fig. 3.8.

The wider and deeper the depletion region the higher the quantum efficiency of photon-electron conversion optimising the responsivity for larger wavelengths with the PIN design. Therefore in case of IR radiation usually silicon PIN types are used.

There is a design trade-off arising from the way a photodiode chip operates. Having high sensitivity for intensity fluctuations requires a large responsivity at the laser wavelength. But then even before saturating, in the sense of nonlinearity occurring in a PIN chip, higher incident power leads to degradation of performance. The average speed at which charge carriers can travel through the depletion region decreases at higher power exposure.
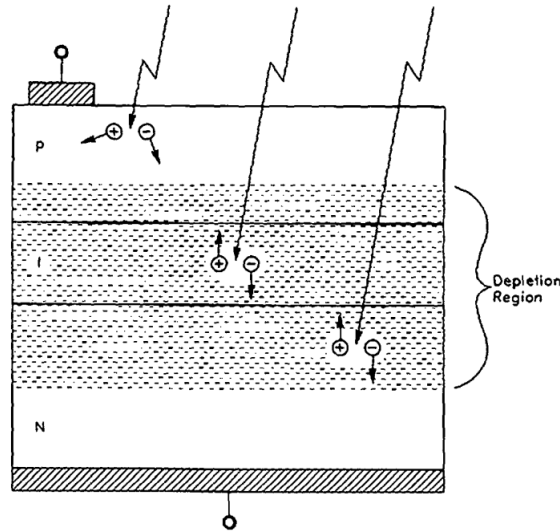

Figure 3.8: PIN photodiode structure. P doped , N-doped and intrinsic layer are marked [31].

The reason is the formation of a charge cloud screening the inner charge carriers from the accelerating electric field. This space charge zone screening is usually compensated by a different design than standard PIN [47], allowing either higher speed or less sensitivity.

Using a BPW-34 PIN chip with responsivity of about 0.6 W/A [32], a factor 2 more than the TPD, leads already at 1 mW exposure in visible degradation of the speed. This effect was noticed by observing the step response in Fig.3.9.
The solution chosen here is to apply close to the maximal specified reverse bias to the chip of 30 V. This brute force approach leads to wearing off the screening by accelerating the outer charges faster out of the depletion region before they accumulate densely to provide screening.[6]

---

[6]Larger reverse bias voltage has to come from an external power supply as the photodiode circuit is going to be driven by our standard ±15 V lab power supplies for safety reasons, necessitating therefore additional noise filtering as explored in appendix B
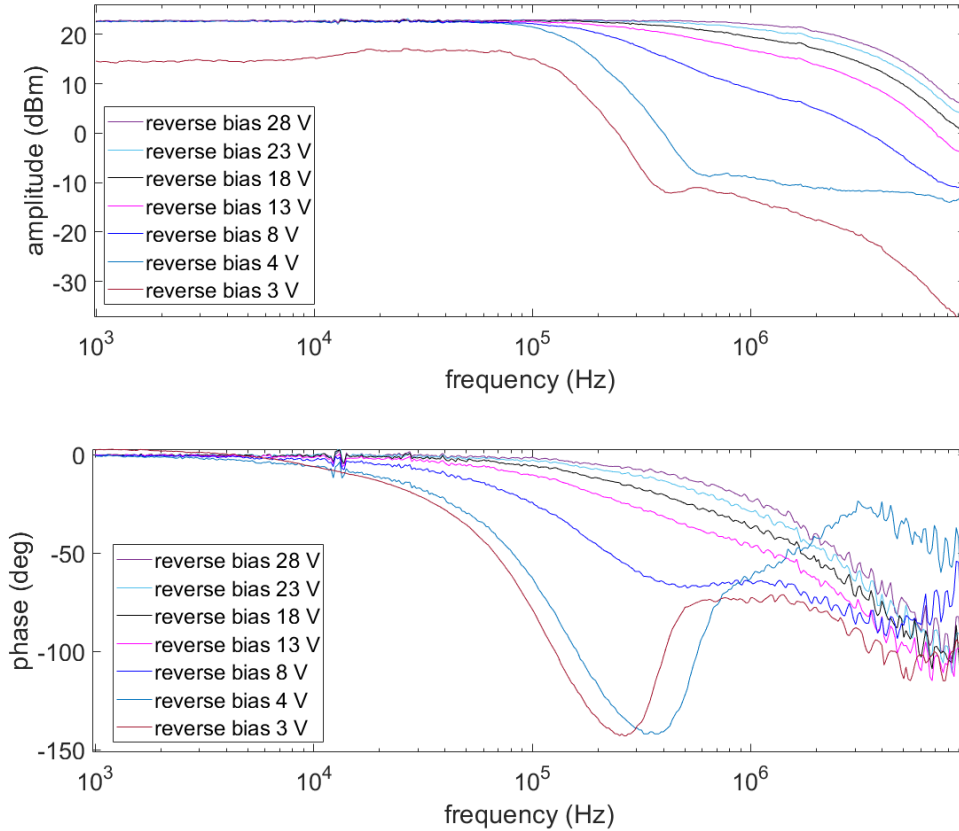
Figure 3.9: Frequency transfer function amplitude and phase of a photodiode circuit with a BPW PIN chip at 1 mW incident power of a 852 nm laser for different reverse biases generated by scalable Voltcraft VLP 1303pro lab power supply.

The setup for measuring this behaviour is the same as the one in the following section which is a replicate of the digital intensity stabilisation in Fig. 3.1. The optical step response was generated by modulating the AOM output intensity with the Keysight module. The laser source is again the 852 nm diode laser.

3.4.4 Performance test

A test was performed to determine the achievable noise suppression as an indicator of the sensitivity of the PD.

If the laser diode operates in single mode it tends to exhibit remarkably low noise. The Moglabs Agile RF Synthesizer ARF021 was employed as a noisier alternative to the Keysight module to add noise. Furthermore an Agilent Technologies oscilloscope signal generator was used to add white noise to the photodiode output. The generate noisier beam as a substitute for the at that moment unavailable TiSa was then stabilised by employing the custom built PD as a sensor for the PID control. Due to the beam splitter light losses the achievable noise stabilisation is limited to 6 dB above shot noise [27, p.231] which was achieved in Fig.3.10 for a certain frequency range indicating shot noise limited detection as aimed for in praxis.
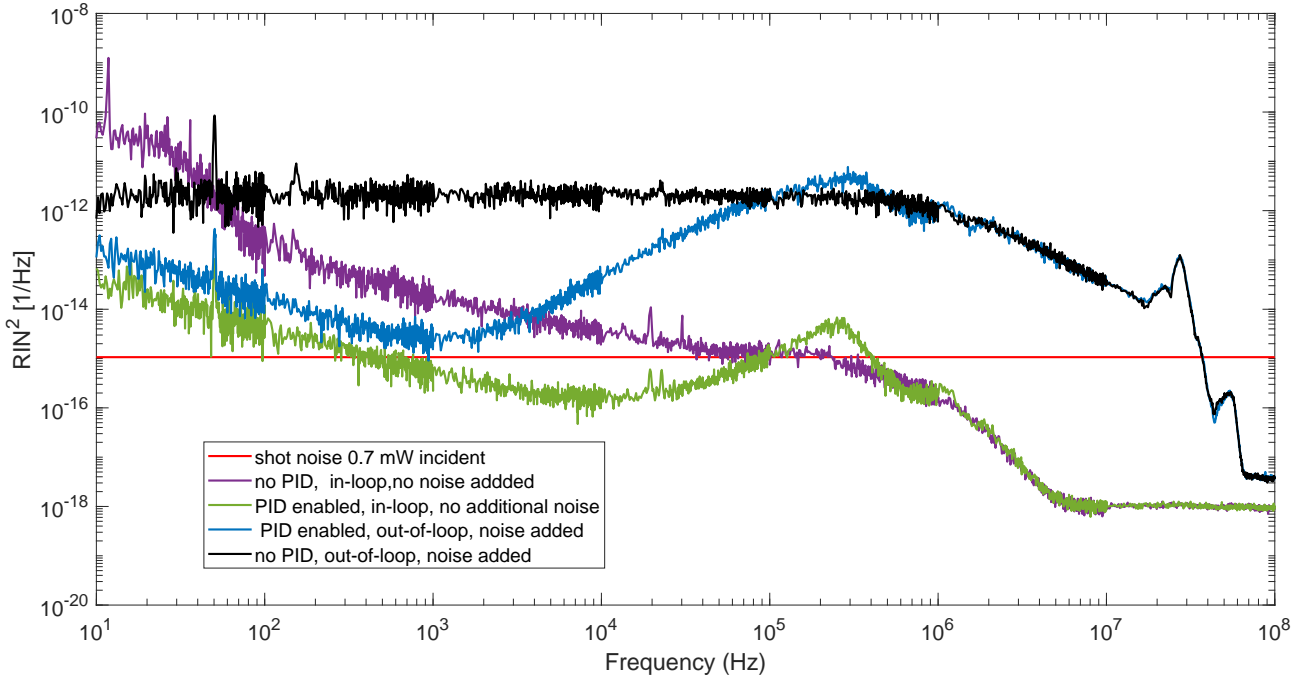
Figure 3.10: Laser intensity stabilisation of a 852 nm diode laser using the Moglabs RF synthesiser with its own PID control. White noise was added externally from an oscilloscope signal generator. Shot noise is reached around a kHz with a suppression of 2 decades in RIN^2.

To summarise this chapter: In order to overcome the limitations arising from the Keysight module's read-out noise, a house-build photodiode amplifier was built and tested. It is possible to regulate down to shot noise with it as shot noise is amplified above the Keysight module's input noise and even with the much higher input noise of the Moglabs digital. This promises ruling out intensity noise as a sizeable effect for decoherence in our setup.

4 COMPRESSION SCHEME

The following chapter deals with the description and analysis of the compression scheme with which the efficiency of plane selection outlined in 2.3.1 may be enhanced. The temporal intensity ramp profile with which atoms are driven to the center of the 3D optical lattice will be studied employing simple estimates. A numerical simulation solving the time dependent Schrödinger equation is then employed to attain robust parameters to test in the experiment and predict the optimum performance. Then first experimental results are going to be summarised and discussed.

The next section describes the basic working principle of release-and-recapture compression [1]. Then key concepts necessary to quantify the limitations and ramp shape will be introduced for a specific compression axis.

4.1 Principle of Compression

The procedure of the release-and-recapture compression is a recently developed experimental technique [58] [71]. The atoms in the HDT plane and along the VDT axis both see a potential of the form of Fig. 4.1 :
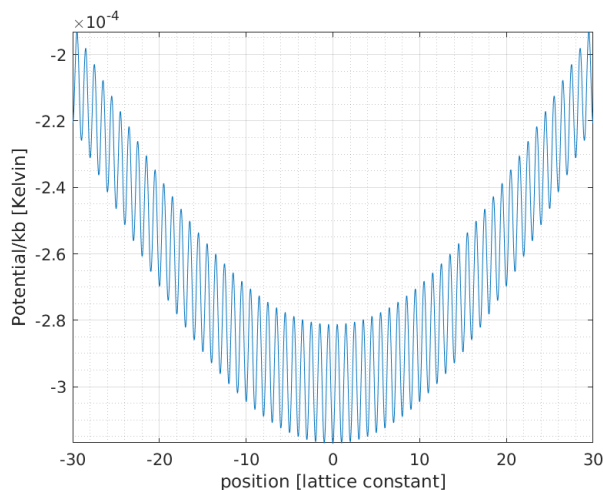

Figure 4.1: Slice of the dipole potential along the orthogonal HDT beam.

The bell shaped potential curve originates from the Gaussian beam profile of the vertical dipole trap in the plot. The lattice is produced by the HDT beams. In case of compression along the vertical direction the roles are reversed : The Gaussian potential then stems from the HDT beams and the lattice from the vertical dipole trap.
The method begins with the ramp down of the lattice beam power and therefore the lattice potential until the atoms are released from the lattice. The Gaussian potential and therefore the VDT beam is kept constant meanwhile. After letting the

---

[1] To stress the difference: what is often referred to as release and recapture procedure in literature is the measurement of the temperature of trapped atoms by measuring the spread of the atomic ensemble for a known release time (for example in [82] or in [38, p.41]). The intensity ramp shape and purpose are entirely different in this case

atoms propagate for a quarter of the trapping period of the harmonic approximation of the Gaussian potential, the lattice is ramped up again. In case the atoms were confined in a region of the Gaussian potential where the harmonic approximation holds, after a quarter period they would all be captured in the center. This holds irrespective to their starting position then.

4.2   Experimental constraints

In the following section the parameters taken from the experiment are summarised. They are used as a basis for estimating the effects of relevance for compression in the rest of this chapter if not otherwise stated.

4.2.1   HDT compression paramters and modelling

Beam powers   The standard experimental parameters are mostly attained from the sideband spectra. The resolvable trapping frequencies in longitudinal direction are about 180 kHz for the VDT, 34 kHz for the orthogonal HDT beam direction and 70 kHz along the two counterpropagating HDT beams. The power can then be inferred by the knowledge of the waist sizes and by Taylor expanding the analytical expression of the potential to second order[8, p.6]. From the power the transversal trapping frequencies are attained, 700 Hz for the VDT and 2 kHz for the HDT beams. The beam powers are 4 W for the VDT and 9 mW for the shallow lattice HDT. As mentioned in section 2.3 the shallow lattice is the lattice depth were transports are conducted.

Beam shape and potential   To calculate the HDT potential, equation 2.1 was used. The intensity profile of the HDT beams is astigmatic (26 µm, vertical direction x 70 µm, horizontal, [7, p.45]). Therefore the modelling of their beam profile was based on an astigmatic Gaussian beam model [72, p.43]. This was done in order to account also for a configuration in which the minimal waist size of 26 µm isn't exactly along the VDT axis. The Gaussian potential of the HDT performing the compression along the vertical direction would differ then in shape. This would affect for example the release duration due to a change of the period of the Gaussian potential.
The vertical potential was similarly calculated based on the approach outlined in [10]. But because of a larger detuning to the relevant transitions ($\lambda = 1064$ nm), it reduced to a much simpler form. The expression has been cross checked with an approximated expression taken from [73, p.106]. This approximative form holds for dipole traps generated by beams far detuned from the hyperfine splitting between ground and excited state of Caesium.

Spatial dimensions   The aim is to compress atoms displaced over a 100 lattice sites in case of the horizontal compression. This constitutes the field of view of the objective using the full NA [7, p.41]. The same goal holds for compressing along the vertical direction. The MOT-lattice overlap procedure when loading atoms into the 3 D lattice, see section 2.2.2, allows estimating the initial spread in this direction

to similarly be about 100 lattice sites. This corresponds to the 1/e width of the MOT, 50 μm [7, p.35].

4.3 Limitations to the compression scheme

In the following sections considerations and limitations for the ramping will be explained. Based on them estimates will be given for a good compression parameter range.

4.3.1 Duration of the compression procedure

The total ramp duration is limited by the lifetime of the atoms within the 3D optical lattice. This leads to lifetimes in the order of seconds due to collisions with the background vapour (see grey curve in Fig.2.13). Because compressing atoms will be part of the standard experimental sequence due to plane selection, the compression scheme needs to be as short as possible. The current target duration is in the order of tens of milliseconds.

4.3.2 Anharmonicity

Atoms further away from the center such that the harmonic approximation does not hold any more won't reach the center in a quarter of the trapping period. The displacement from the center for the horizontal compression starts to become relevant at 15 lattice sites initial displacement (Fig.4.2).
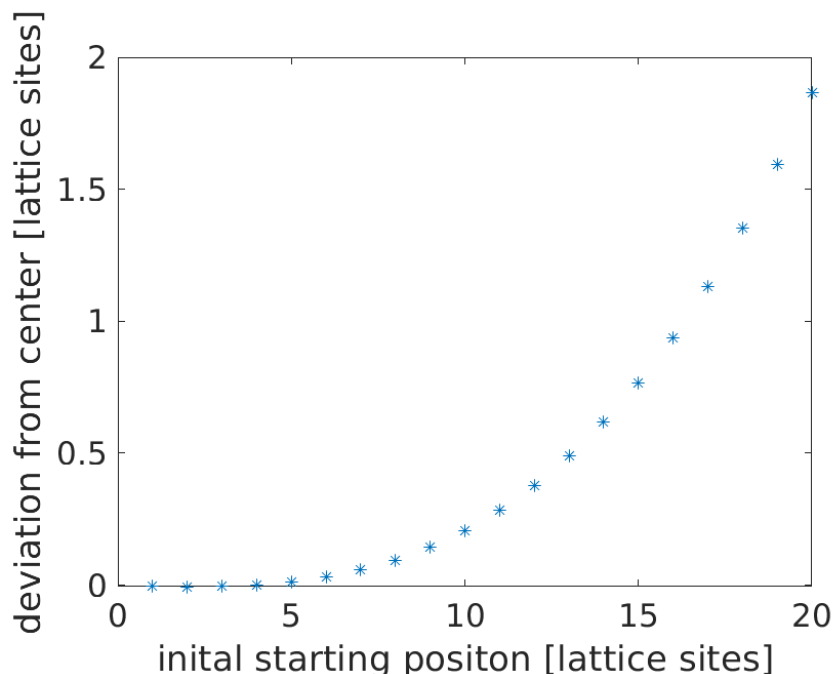
Figure 4.2: Simulated mean position of an atom initialised in the vibrational ground state of different lattice sites after instantaneous ramp down of the HDT lattice and waiting for a quarter period of the VDT. Using parameters of section 4.2.1

In case of the vertical compression, anharmonicity becomes relevant at about 6 lattice sites displacement from the center. The reason for this difference lies in the

much shallower Gaussian potential generated by the HDT beams. When Taylor expanding the Gaussian intensity profile the next highest correction term scales with $O((\frac{\Delta x}{w_0})^4)$. With waist size of $w_0 = 26\,\mu m$ the horizontal beams Gaussian potential is only for smaller distances Δx harmonic compared to the VDT's $w_0 = 77\,\mu m$ waist along horizontal axes. This reduces the validity range of the harmonic approximation in vertical compressions.

As a consequence multiple compressions ramp need to be run in series.

4.3.3 Liouville theorem limit

Another limitation to compression can be motivated by classical physics. In case of compression the increase in density leads to an increase in momentum for a cloud of particles. This holds for dynamics that can be described by Hamilton mechanics. This notion of phase space volume conversation is formalised as Liouville's theorem[81, p.68]. Liouville's theorem also holds for time dependent Hamiltonians (so also during the ramp down).
Where it does not hold is when dissipative or say velocity dependent forces are at work due to the system not being described by Hamilton mechanics any more. In our case the dissipative force is cooling, as in section 2.2.1 introduced. Therefore cooling into the ground state is necessary not only before the first compression ramp, but before each successive ramp.

4.3.4 Adiabaticity

While ramping down the lattice potential it is in principle advantageous to remain adiabatic such that the atomic wave function can follow the potential. In the following section the applied definition of adiabaticity will be clarified. Then the argument for staying mostly adiabatic during ramp down will be discussed.

Adiabatic approximation The adiabatic theorem states that if a particle in a system with discrete eigenenergies is initialised in an eigenstate $|j(t = 0)\rangle$ (in the sense of the j'th numbered eigenstate of the system, $j \in \mathbb{N} \cup \{0\}$) then during an infitesimally slow change of the Hamiltonian H it will remain in the instantenous eigenstate $|j(t)\rangle$ over the duration T of change [75]. A simple condition which overestimates the violation of adiabaticity follows from [76, p.754] and is modified by [86] in units of $s = t/t_f$:

$$\max_{t \in [0,T]} \frac{\hbar}{t_f} \frac{\mid \langle i | \frac{\partial H}{\partial s} | j \rangle \mid}{\mid E_i - E_j \mid^2} \ll 1 \tag{4.1}$$

where t_f is a parameter introduced such that when rewriting the Hamoltionian in terms of s, t_f does not explicitly appear in it. This is a modification of the classical criteria used in [76, p.754] to formally exclude Hamiltonians with more than one characteristic time scale. Otherwise adiabaticity cannot be estimated with inequalitys like this [79]. It still holds in systems with only one relevant time scale [80, p.6] such as in optical lattices before tunnelling becomes important for the dynamics. Staying adiabatic within the procedure is advantageous, since the spread of the atom poitions distribution is limited during the release.

If the initial ground state is able to follow the lowering of the lattice potential adiabatically, its instantaneous trapping frequency will decrease over time. For shallow lattices violating the harmonicity assumption [51, p.19], similarly the relevant time scale decreases. As long as tunnelling is negligible, the width in the momentum representation of the ground state decreases, similar to the harmonic case. There the standard deviation (std) of the momentum space represented ground state is $\sqrt{\hbar\omega_{\mathrm{tr}}m}$. During the release time of a quarter period of the harmonically approximated Gaussian potential the spatial broadening of the ground state depends on the initial momentum distribution. For a Gaussian wave packet released in free space for example holds [83, p.2]:

$$\Delta x(t) = \sqrt{(\Delta x(t_0)^2 + \frac{\Delta p(t_0)t^2}{2m_{cs}})} \qquad ,\tag{4.2}$$

with t_0 the point in time when the release took place[2]. Therefore broadening of the wave function during the release is going to be minimised by reducing the initial momentum width before release. This can be achieved by ramping as low as possible and adiabatically long for the wave function to follow.

Adiabatic ramp shape Based on the inequality 4.1 and using the harmonic approximation one can estimate the ramp shape that violates adiabaticity the least [38, p.44][3] [38]. The idea is that an appropriate ramp function should follow a shape that leaves the left hand side of inequality 4.1 constant in time and using a polynomial ansatz t^n, $n \in \mathbb{Z}$ results in hyperbolic shape in this case.
Following [38, p.45] a parabolic ramp down in a less critical trap depth region will be performed to speed up the overall ramping duration.

---

[2]The position-momentum correlation terms cancel out for a Gaussian function

[3]During turning off the potential the trapping frequency goes to zero and therefore the time scale required for adiabaticity diverges
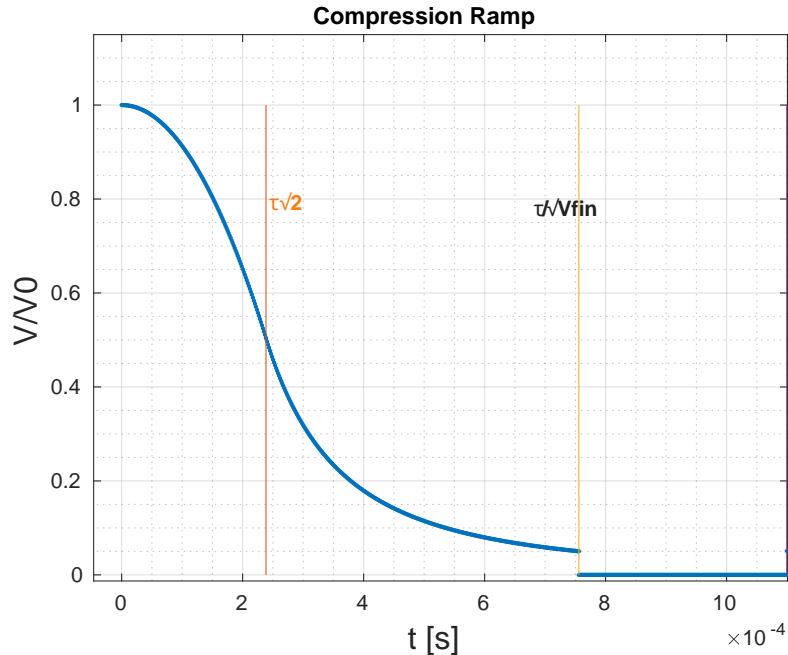
Figure 4.3: Example ramp for the adiabatic lowering of the lattice with lowering time t against instantaneous trap depth $V(t)$ in terms of the initial trap depth V_0. Recapture would be the same ramp shape mirrored and scaled by a factor in its characteristic time τ to speed up the capture. The lowest relative potential depth in our setup, Vfin, is limited to 10^{-4}. This is the EOM extinction ratio within the intensity stabilisation setup of Fig. 3.1 for the HDT beams.

The ramps are characterised by the time scale τ where $\tau\sqrt{2}$ is the point in time for transitioning from parabolic to hyperbolic ramp down. The time where the lattice is entirely shut off to start the release is $\frac{\tau}{\sqrt{V_{fin}}}$, with V_{fin} the relative trap depth before shutting off.

A shut off has to be performed to avoid tunnelling and start a well defined release time. A ramp down along the orthogonal HDT axis will have to be slower than along the counterpropagating beam direction due to the smaller trapping frequency. In the harmonic approximation the trapping frequency sets the time scale for to respect adiabaticity. For this reason the estimates and simulation will concentrate in the following on compression along this slow axis.

4.3.5 Introducing lattice dynamics

Critical trap depths for adiabaticity In order to make use of inequality 3.1 the following assumptions are going to be introduced to attain approximative solutions for $|i\rangle , |j\rangle$ and E_i and E_j that can be inserted. Due to the Ramp shape only the hyperbolic ramp down will be considered. The reason being that adiabaticity is more likely to be violated the shallower the lattice is. This is due to the fact that the trapping frequency for vanishing potentials vanishes and therefore the time scale for which one needs to be slower to stay adiabatic diverges. This holds even in the non-harmonic trap depth regime as will be elaborated later in this section.

To estimate how well adiabaticity will be maintained neglecting the Gaussian potential, a simplified model will be introduced. Only then inequality 3.1 would be

applicable.

This will be accomplished by first introducing a simplified model of the potential for the orthogonal beam axis. The Mathieu equation will then be recognised within it and its characteristics summarised. This is followed by a brief outline of solid state physical concepts. Then this section concludes with presenting the validity range of neglecting the VDT Gaussian potential.

Model describing the lattice dynamics   The first simplification is Taylor expanding the VDT Gaussian potential up to second order. This restricts the validity of the estimate to about ± 12 lattice sites from the center in case of compression along the HDT2 axis for the given parameters following Fig. 4.2. The second approximation is treating the HDT potential as a $\sin^2$ potential. This holds approximately if all HDT beam powers are the same and if one restricts the treatment to along the orthogonal beam axis only. Along the counterpropagating axis for example the potential is unsinusoidal , Fig. 4.4.
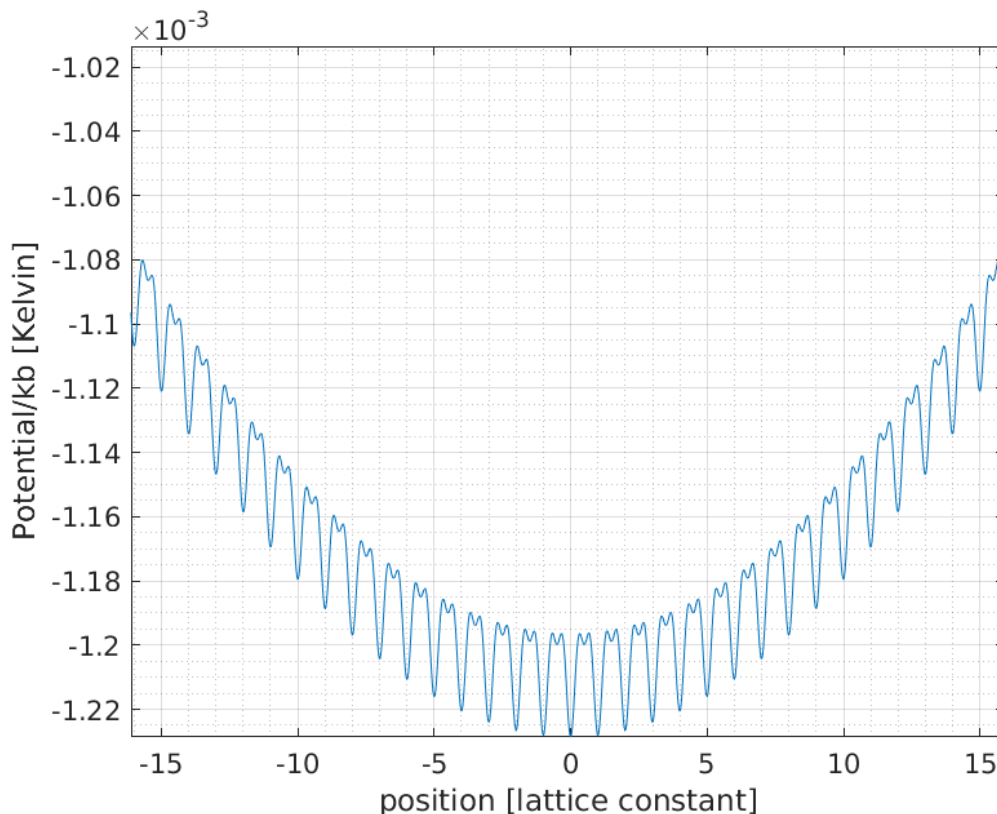

Figure 4.4: Potential along HDT1,3 axis for the parameters given in 3.2.1.

The deviation from the sine shape generally happens at higher trap depths in which atoms are not likely to be. In addition if the slower axis is adiabatic the faster axis will be too. Therefore it may be neglected for now.

The following Schrödinger equation arises from this model :

$$\hbar i \frac{\partial \psi(x,t)}{\partial t} = \left(\overbrace{-\frac{\hbar^2}{2m_{Cs}} \frac{\partial^2}{\partial \tilde{x}^2} + V_0 \sin^2\left(x\frac{\pi}{d}\right)}^{H_0} + \frac{m_{Cs}\omega_{gauss}^2 x^2}{2} \right) \psi(x,t) \qquad , \quad (4.3)$$

with d the lattice constant. Ignoring the harmonic part for the moment, the stationary Schrödinger equation of H_0 can be reformulated into the so called Mathieu equation following [19, pp.423-424].

$$\frac{d^2}{d\tilde{x}^2}\tilde{\psi}(\tilde{x},t) + (o - 2q\cos(2\tilde{x}))\tilde{\psi}(\tilde{x},t) = 0 \qquad (4.4)$$

with dimensionless eigenenergy $o = (2E - V_0)/(2E_R)$, dimensionless potential $q = -V_0/(4E_R)$, recoil energy $E_R = \frac{\hbar^2\pi^2}{2m_{Cs}d^2}$ and $\tilde{x} = x\frac{\pi}{d}$. The behaviour of the Mathieu equations is well studied and the solutions are available as built-in functions in Mathematica[87].

One usually differentiate between even, $C(a,q,\tilde{x})$, and odd Mathieu functions $S(b,q,\tilde{x})$ as eigensolutions. For $q = 0$ they are just a cosine and a sine function while for $q > 0$ only for characteristic eigenergies o , called $a(\tilde{k},q)$ and $b(\tilde{k},q)$, the even and odd Mathieu functions are periodic in $\tilde{x}$ and $\tilde{k} \in \mathbb{R}$. They shall then be denoted as $ce(a,\tilde{x},q)$ and $se(b,\tilde{x},q)$. For periodic boundary conditions and a periodic potential the solutions can always be written in terms of Bloch waves following Bloch's theorem. A Bloch wave shall be denoted as $\phi_k(\tilde{x},t) = u_k(\tilde{x},t)\exp(ik\tilde{x})$ with $u_k(\tilde{x},t)$ a lattice periodic function and k the dimensionless quasimomentum. This defines the width of the Brillouin zone (BZ) based on π-periodic $\tilde{x}$ and reciprocal lattice vector magnitude $k_B = \frac{2\pi}{x_B} = 2$, so $k \in [-1,1]$. The Mathieu functions exhibit in their eigenenergy spectrum a band structure when plotted against the quasimomentum. Using the parameters of section 4.2.1 and a representation reduced to the first BZ leads to Fig. 4.5.
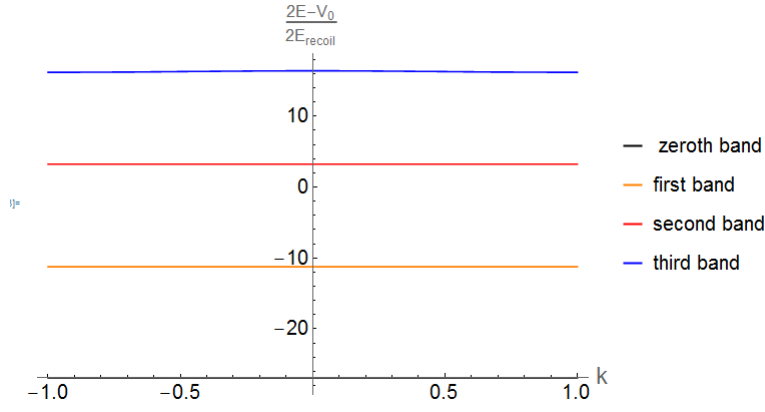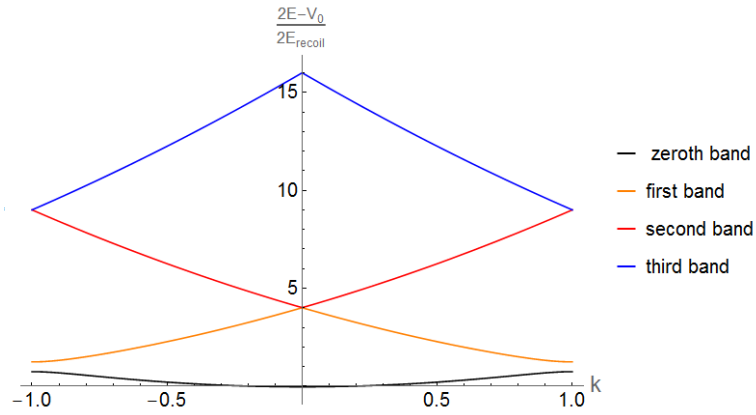
Figure 4.5: a)Eigenenergy in dependence of the quasimomentum for a lattice trapping frequency of 35 kHz in the harmonic approximation. The plot was generated by plotting the even eigenergy $a(k, -V_0/4)$ for the given V_0 of section 4.2.1 over 4 Brillouin lengths and folding back into the first Brillouin zone. In the harmonic limit the bands are flat and the distance between the bands is 69 recoils or $h\,35\,\mathrm{kHz}$. Flat bands correspond to a good harmonic approximation b) Eigenenergy in dependence of the quasimomentum for a trap depth of 1 recoil. The bands are increasingly less flat the shallower the lattice is. Harmonicity does not hold in this case well.

The characteristic time scale of the Hamiltonian itself is for all trap depth regimes given by the the band gap at the edge of the Brillouin zone. In the deep lattice with flat bands for all k it is the vibrational level spacing and therefore the trap frequency while in the quasi free regime it determines the tunnelling rate, as will be discussed in this section. One can therefore generalise to an effective time scale beyond the validity of the harmonic approximation based on the band gap at the edge.
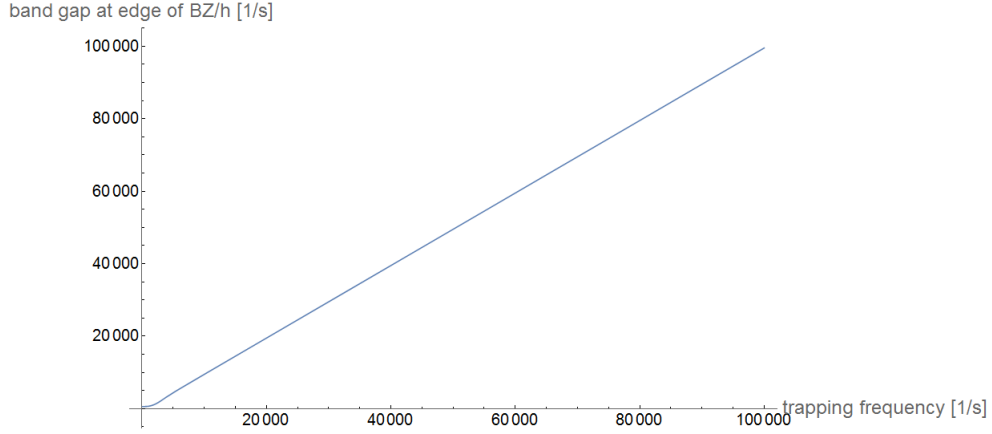
Figure 4.6: Band gap frequency in dependence on the trapping frequency.

Depending on the treatment of the periodic potential it is convenient to introduce a different function base from the Bloch waves. The localised Wannier functions $w_s(\tilde{x} - j\pi, t)$, s the band index and lattice site $j \in \mathbb{Z}$, can be constructed by Bloch waves the following way[51, p.18]. They can be chosen to be real functions.

$$w^s(\tilde{x} - j\pi) = \int_{-1}^{1} \mathrm{d}k \exp(-ik(\tilde{x} - j\pi))\phi_k^s(\tilde{x}) \tag{4.5}$$

Neglecting the Gaussian potential Now coming back to equation 4.3: In order to exclude the harmonic potential the connection between the Mathieu equaion and its solutions and the actual Hamiltonian of equation 4.3 will be closely following the discussion in [84]. The restriction to be applied to further simplify the estimate is then expressing $\psi(x,t)$ in terms of the lowest band Wannier functions only.

$$\psi(x,t) = \sum_j z_j(t)w_0(\tilde{x} - j\pi) \tag{4.6}$$

For lattice depths above $2E_R$ next to nearest neighbour hopping is negligible by an order of magnitude. With only nearest neighbour hopping the tight binding regime is formally defined and in this case inserting 4.6 in 4.3 leads to the following equation of motion for the expansion coefficients $z_j(x,t)$:

$$\frac{\partial z_j}{\partial t} = -J(z_{j+1} + z_{j-1}) + \Omega j^2 z_j + \epsilon_j z_j \qquad , \tag{4.7}$$

with $\Omega = \frac{1}{2}m_{Cs}d^2\omega_{gauss}^2$, ϵ_j the on-site energy and J the Mathieu equation hopping matrix element or

$$J = -\int \mathrm{d}x w_0(\tilde{x})H_0 w_0(\tilde{x} - j\pi) \tag{4.8}$$

The orthonormality condition of the Wannier states was used here[51, p.18]:

$$\int \mathrm{d}x w^s(\tilde{x} - j\pi)w^{s'}(\tilde{x} - j'\pi) = \delta_{s,s'}\delta_{j,j'} \tag{4.9}$$

Applying an exponential ansatz for the m-th eigenstate for z_j so $z_j^m(t) = f_j^m \exp(-iE_m t/\hbar)$ leads to a recursion relation satisfied by the π periodic Mathieu functions. For $r = 0, 1, 2, 3, ..$ the even and odd eigenenergies are:

$$E_{2r} = \frac{\Omega}{4}a(2r, 4J/\Omega)$$

$$E_{2r+1} = \frac{\Omega}{4}b(2r, 4J/\Omega) \tag{4.10}$$

Higher energy eigenstates in this case refers to excitations within the vibrational energy spectrum of the VDT Gaussian potential. So in order to neglect this potential it is necessary to exclude transitions within its vibrational structure so $\frac{E_1 - E_0}{E_0} \gg 1 \Rightarrow \frac{b(0, 4J/\Omega)}{a(0, 4J/\Omega)} \gg 1$. This in turn holds for $4J/\Omega \gg 1$. In the tight binding regime furthermore holds that the hopping matrix element J can be approximated by the height of the lowest band, so $J/4 = E(k=1) - E(k=0)$ [85, p.897].
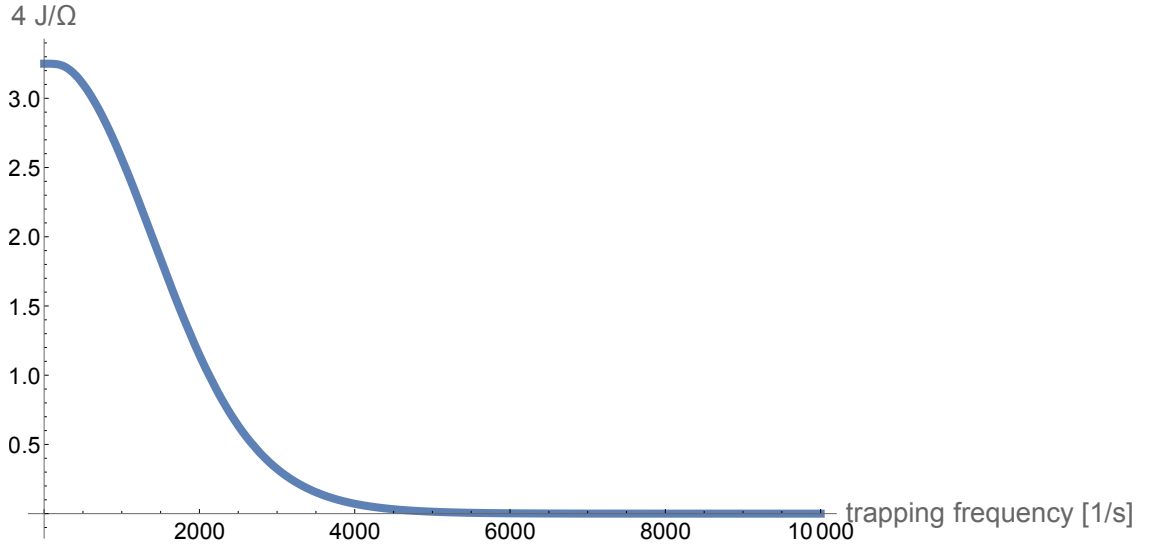

Figure 4.7: Hopping matrix element divided by the energy shift due to the VDT harmonic potential per site plotted against the HDT lattice trapping frequency.

Based on Fig. 4.7 the measure $4J/\Omega$ will be within the experimental parameters always in about the order of magnitude of 1. Therefore a treatment neglecting the vertical dipole potential and only concerning oneself with the lattice is insufficient in estimating the ramp parameters reliably. But it will be fruitful to gain a deeper understanding of the physical scales governing adiabaticity in the system.

Adiabaticity estimate   After the discussion about the validity for applying inequality 4.1 on only the Mathieu equation part of the Hamiltonian, the evaluation will be attempted. The measure of when ramp parameter τ and minimal potential depth V_{fin} violate adiabaticity requires first determining how each term in inequality 4.1 is made up of.
As a first approximation the violation of adiabaticity will be the strongest at the point in time when turning off the lattice potential. The total ramp down time T neglecting the parabolic ramp part is is given by $\frac{\tau}{\sqrt{V_{fin}/V_0}}$. The characteristic time scale of the external process changing the Hamiltonian t_f is just τ due to the ramp shape.
The energy spacing between different bands arises from the Mathieu eigenvalues. For deeper lattices the bands are flat but for shallower lattices the smallest band gap

is at the edge of the Brillouin zone. To get a worst case estimate the energy spacing will be substituted by the spacing at the edge. This also matches the intuition that this energy scale is closely related to the characteristic time scale of the system as stated. The $|i\rangle$, $|j\rangle$ are the vibrational eigenstate functions of the respective bands They will be assumed to be (Bloch-) Wannier functions. Note that they are time dependent due to the change of the potential in time. Inserting this in inequality 4.1 leads to

$$1 \gg \max_{t \in [0,T]} \frac{\hbar}{t_f} \frac{\mid \langle i| \frac{\partial H}{\partial s} |j\rangle \mid}{\mid E_i - E_j \mid^2} \approx \frac{\hbar}{\tau E_R^2} \frac{\mid \int_{-\infty}^{\infty} w_i(x,T) V_0 \frac{\tau^3}{T^3} \sin^2(kx) w_j(x,T) \mid \mathrm{d}x}{\mid a(2, -V_0 \frac{\tau^2}{T^2}/(4E_R)) - a(1, -V_0 \frac{\tau^2}{T^2}/(4E_R)) \mid^2} \equiv \beta(V_0, \tau, T)$$

(4.11)

here the real-valueness of the Wannier functions was employed. In addition the expectation was utilised that right before turning off the lattice, violation of adiabaticity is assumed to be the strongest . The integral will be zero unless $j = i + 2n$, , $n \in \mathbb{N}$, due to symmetry. Restricting the calculation to only j = 2 for simplicity, β will become an approximation to gain intuition for the time scales of adiabaticity. But is not an accurate estimate for the compression with VDT turned on. A more complete description allowing for this case an estimate would be based on employing Wannier-Stark functions. Instead of neglecting the Gaussian envelope it would be linearised, treating it as a tilting of the lattice in first order [29, pp.64-64].

4.3.6 Minimal momentum spread

There is an additional limit to how much ramp down is practical based on the adiabaticity argument of section 4.3. The initial vibrational ground state is as was mentioned before approximately the lowest band Wannier state. It is defined by a superposition in equal parts of all the lowest band Bloch vectors of the first BZ (equation 4.5). This means its quasimomentum distribution is a flat top profile filling homogenously the first BZ. During an adiabatic ramp down the quasimomentum is not only conserved but in the shallow lattice also projected on the physical momentum [88]. It is not possible with further ramp down to narrow the width of the atom's momentum wave function to lower values than this. With this minimal momentum spread one can estimate a minimal spatial spread of 1.5 lattice sites during release: $hT_{trap,VDT}/(4m_{Cs}c) \approx 1.5d$. This estimate and the one of the following section will be employed to study the effects of broadening within the stated approximations in section 4.4.2.

4.3.7 Broadening during ramp down

The widening during release is estimated in equation 4.2 for a harmonic oscillator ground state state or a Gaussian wave packet. But before that, an increase in the width during the lattice lowering may be expected due to the crystal momentum dispersion $\Delta x_\tau = \int_0^T \frac{\partial E}{\partial k} \frac{d}{\pi \hbar} \mathrm{d}t$. Assuming an upper bound for the derivative by averaging the slope in the BZ allows substituting the widening by

$$\Delta x_\tau \approx \int_0^T \mathrm{d}t \frac{2(E(k=1, t=T) - E(k=0, t=T))}{\pi d \hbar} \qquad , \qquad (4.12)$$

while the crystal momentum in deeper lattices is negligible due to the flat band structure.

4.3.8 Tunnelling

Another detrimental effect to the compression scheme is tunnelling. It is not possible to reduce the width of the spatial position distribution after release. So tunnelling before release will always add additional width which in itself expands again during ramp down. In addition it effectively washes out the point in time of release. Two different approaches may be employed to estimate the tunnelling rate.

One is the Wenzel-Kramers-Brillouin approximation (WKB), the other is the tunnel rate estimate based on the hopping matrix element. The WKB approximation is based on assuming a spatially weakly varying potential. The approximation is used when solving the underlying time independent Schrödinger equation by making a plane wave ansatz. Then spatial varying amplitudes and phases are assumed. Such an ansatz when treating the transmission through a potential barrier results in an estimate of the tunnelling probability of the form [90, p.322]

$$P_{tunnel} = \exp(-\frac{2}{\hbar} \int_0^a |p(x)| \, \mathrm{d}x), \qquad , \qquad (4.13)$$

with a the length of the non-classical region and $p = \sqrt{2m(V(x) - E)}$. From the tunnelling probability the tunnelling rate may be approximated as tunnel probability times frequency of impinging on the barrier or tunnel rate $= P_{tunnel}\omega_{trap}$ in our case, following [90, p.338]. Attaining this way the tunnel rate based on the WKB approximation allows comparing it with the hopping matrix element. Both estimates agree well.
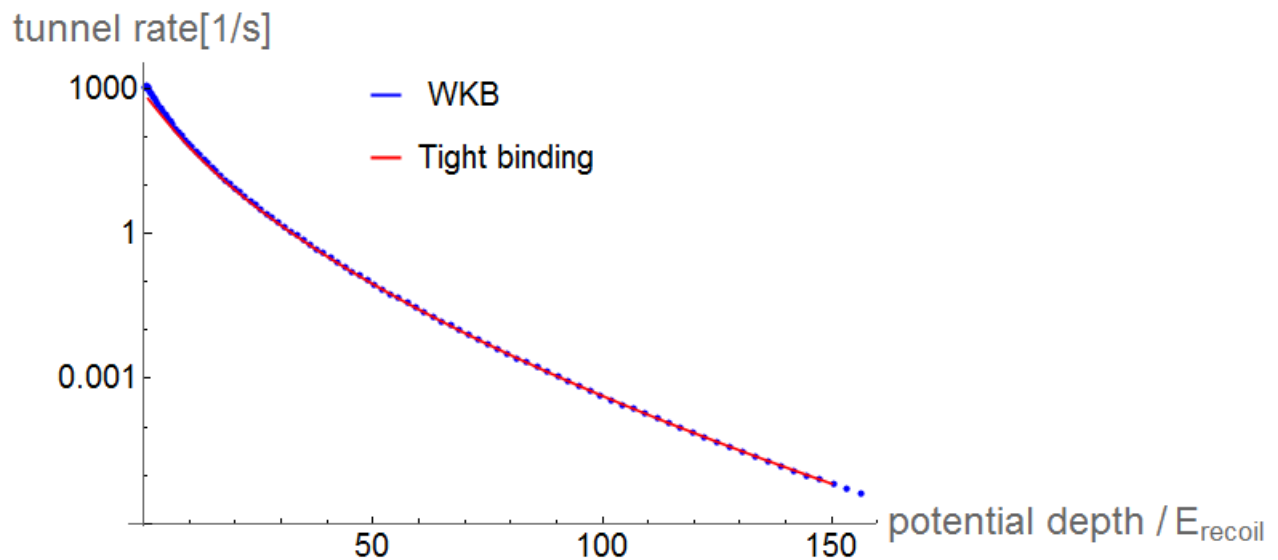

Figure 4.8: Tunnel rate in dependence of the HDT beam power neglecting the VDT. Red curve based on the hopping matrix element and the blue curve is based on the WKB approximation.

The break down for this estimate is at about 2 recoils. This can be illustrated by observing the WKB tunnelling probability is above one. The approximation breaks down when the tunnelling probability becomes significant. This is in the same regime where next-nearest neighbour hopping cannot be neglected following [84].
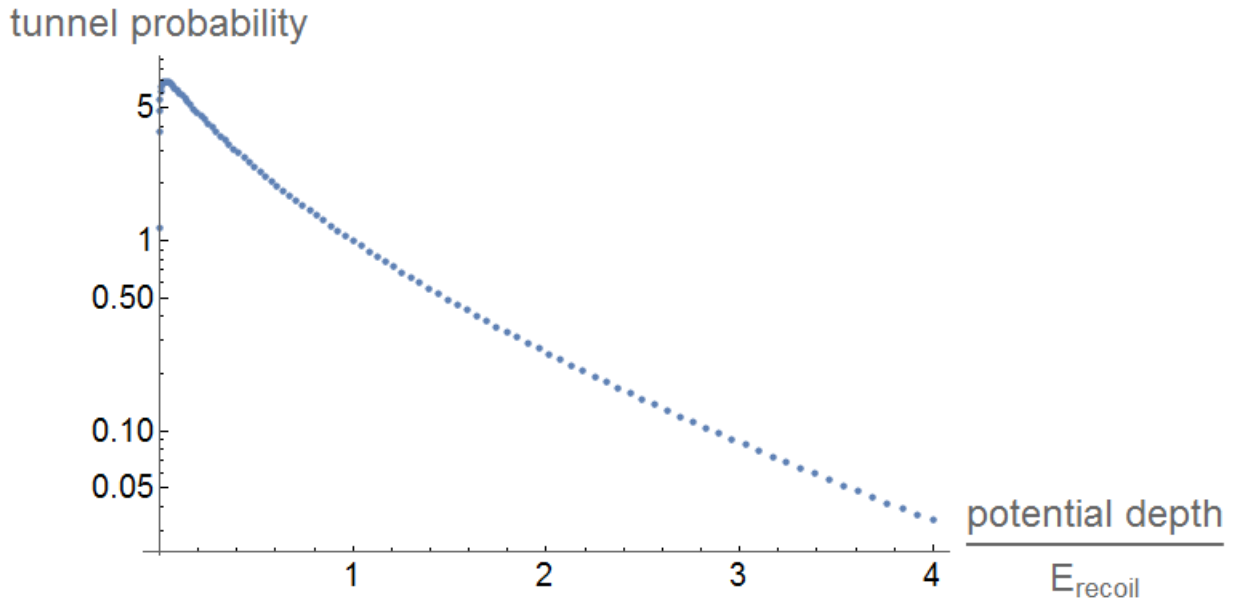
Figure 4.9: Tunnel probability of the WKB method. It breaks down at about 2 recoils where next-nearest neighbour hopping becomes significant.

So reducing the V_{fin} to less than say 5 recoils is creating a significant spread over at least 2 lattice sites before release.

4.4 Summary simulation

Due to heating and influences from the optical lattice, a classical simulation of the process does not suffice to get an estimate of the compression. In addition the effect of ramping adiabatically and tunnelling can't be understood classically. In order to perform a quantum mechanical treatment of the compression, the time dependent Schrödinger equation has been solved. For further details for this refer to appendix C.

The simulation assumes at the beginning a single atom displaced by say 12 lattice sites in the vibrational ground state.

The compression is then performed while ensuring numerical stability which is measured by the norm deviation. The reason is that the way the Schrödinger equation is solved does not strictly fulfil unitary evolution of the wave packets. So unphysical states with norm different from 1 are related to a bad simulation parameter choice, either concerning the time grid or the space grid.

4.4.1 Simulation analysis

The measure of merit for the compression success is the standard deviation of the probability distribution of the atoms. It is not calculated relative to the mean position. Because of the aim of compressing in the center the standard deviation employed here is the average rms distance from the center weighted by each lattice sites integrated probability. In other words the measure of merit is the momentum of inertia relative to the center.

The simulation sequence consists of ramping down, release and ramping up. In

46

addition a waiting period as long as the release time is performed. The purpose of this waiting period ensures that the atoms don't gain enough kinetic energy due to fast ramping up to escape the central lattice sites after the end of the ramp up.

Successive compressions are analysed by starting with a single compression ramp. For each initialised lattice site the final distribution will be stored within a matrix $\hat{M}$ after integrating the probability density per lattice site . By scanning all initial positions $\hat{M}$ would contain all information of the ramp performance given the potential shape.

Multiplying such matrices allows fast simulation of successive ramps with in-between ground state cooling.

4.4.2 Comparison simulation with estimate

We estimate the spatial width after ramp down and release at time t_0 by breaking it down the following way: Assuming adiabaticity to hold, the initial width is given partly by the width of the harmonic oscillator ground state of the release depth Vfin, $\Delta x(t_0)_{harm} = \sqrt{\frac{\hbar}{m_{Cs}\omega(t=t_0)}}$. In addition during ramp down the atom will have experienced broadening due to its crystal momentum by Δx_τ from section 4.12. Those two widths will be for simplicity linearly added together to constitute the entire position spread $\Delta x(t_0)_{tot} = \Delta x(t_0)_{harm} + \Delta x_\tau$.

The momentum spread before release similarly consists of the harmonic part being $\Delta p(t_0)_{harm} = \sqrt{\hbar m_{cs}\omega}$. The momentum broadening arising from Δx_τ using the uncertainty relation is $\Delta p_\tau = \frac{\hbar}{2\Delta x_\tau}$. The absolute minimum momentum width of one homogeneously filled BZ in case of adiabatic mapping , $\Delta p_{lattice} = \frac{2\pi\hbar}{d}$ will be moreover considered.

Adding the momenta broadening together linearly to attain a $\Delta p(t_0)_{tot}$, equation 4.2 may be used to estimate the additional broadening during release. The result of this estimate can be seen in Fig. 4.10 a). There is no dependency of the std as a measure of final compression on τ. This is due to assuming adiabaticity a priori and in addition the broadening effect of Δx_τ is not significant. The reason for this lies in the fact that the dispersion relation from which Δx_τ stems is rather flat in deeper lattices. The duration the ramp stays in shallower lattices on the other hand is not comparable to the release time in scale. To give an idea of scaling, a good choice of τ which respects adiabaticity is of the order of the inverse of the lattice trapping frequency. Therefore in this case of the order of tens of microseconds whereas the release time is of the order of ms in case of horizontal compression.

The estimate for the broadening during release is also not taking into account tunnelling which leads to continuous improvement when lowering the release depth. The measure of adiabaticity β is calculated based on section 4.3.5 only considering overlap of the ground state with the second excited state. The critical value for adiabaticity was chosen to be about 0.1 and has been added to Fig.4.10 to complement the estimate of broadening. The same holds for marking the trap depth of a critical tunnelling probability. Comparing Fig. 4.10 a) with Fig. 4.10 b) shows the precision of the adiabaticity estimate applied to the lattice dynamics without any Gaussian potential envelope.
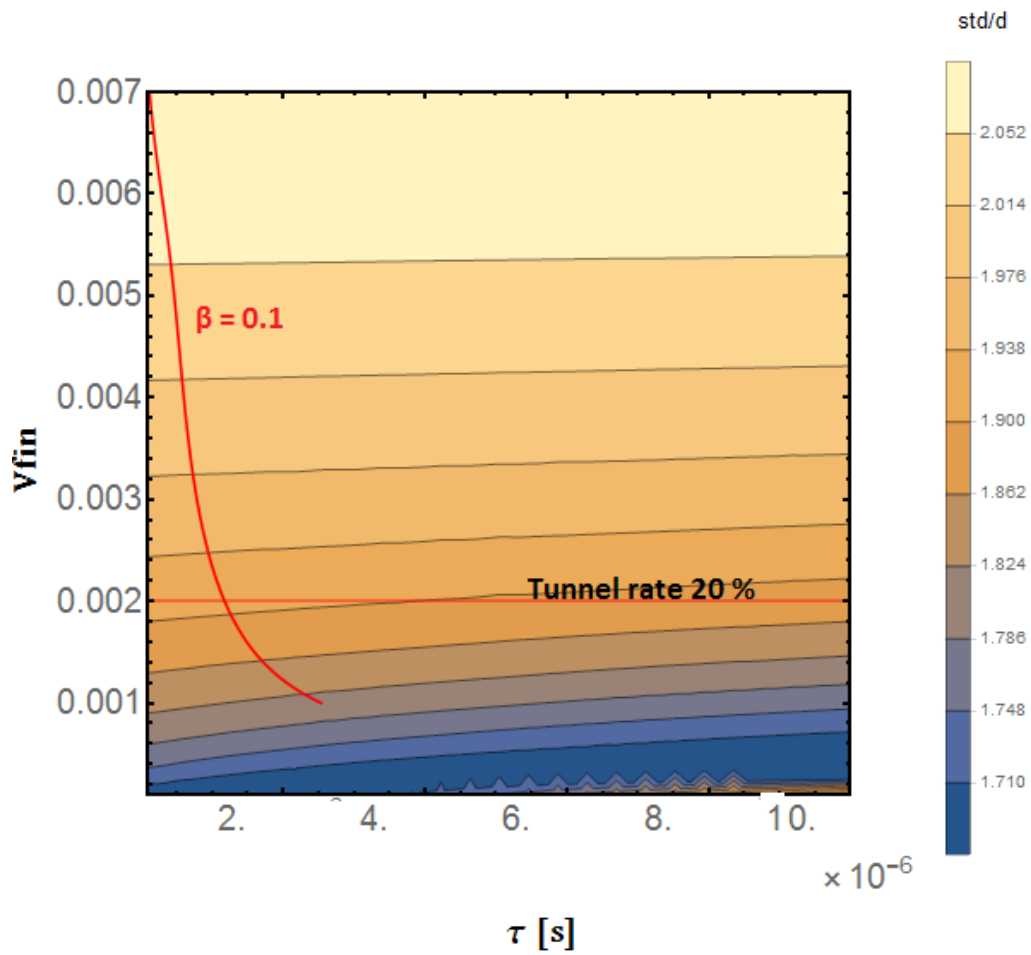
4.10 a) Estimated broadening based on 4.4.1 . $\beta = 0.1$ is the indicator of adiabaticity. Critical trap depth for the tunnelling has been marked.
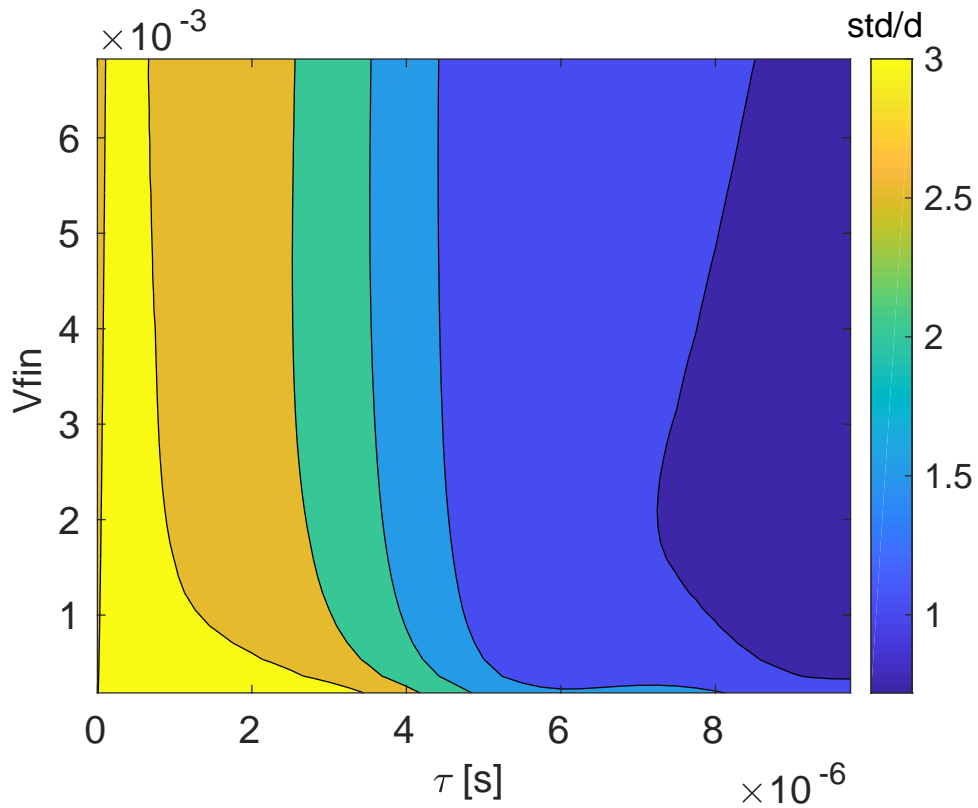
4.10 b) Simulation result without VDT turned on.

The region where adiabaticity may be critical according to the β estimates agrees with the simulated plot 4.10 b). Additional broadening can be observed and traced back to the wave function not being able to follow the potential broadening fast enough.

4.4.3 Introducing Gaussian potential in simulation

Having understood well the situation without Gaussian potential the following section deals with exploring the differences briefly that follow from its presence. In addition the ramping scheme for the setup will be judged in terms of how well an optimal ramp may be intensity noise insensitive. In addition the caveat of compression along the horizontal plane which involves a faster and a slower axis will be discussed.

Effect of the Gaussian potential The effect of the Gaussian potential may not be neglected following section 4.3.5. So large deviation from the parameter landscape of the last section may be expected .
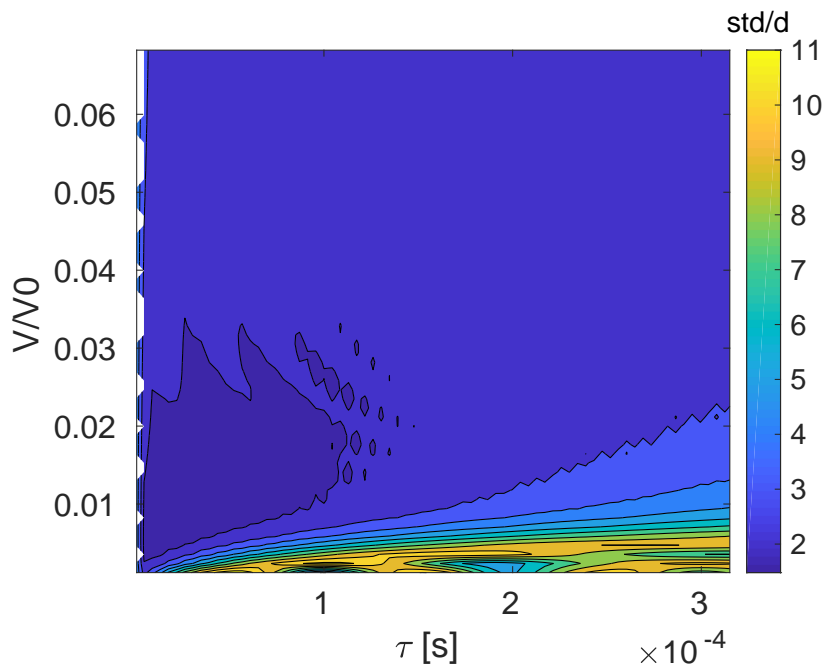

Figure 4.11: Atom initialised in the ground state, 12 lattice sites displaced along HDT2 from the center for different ramp characteristic time τ and release depth V_{fin}. The std was plotted in dependence of τ and V_{fin}. The vertical beam power was lowered to only 15 % or about 600 mW . The reason being that a high slope of the VDT leads to low capturing rate due to atoms gaining large momenta in the center of the HDT following simulations.
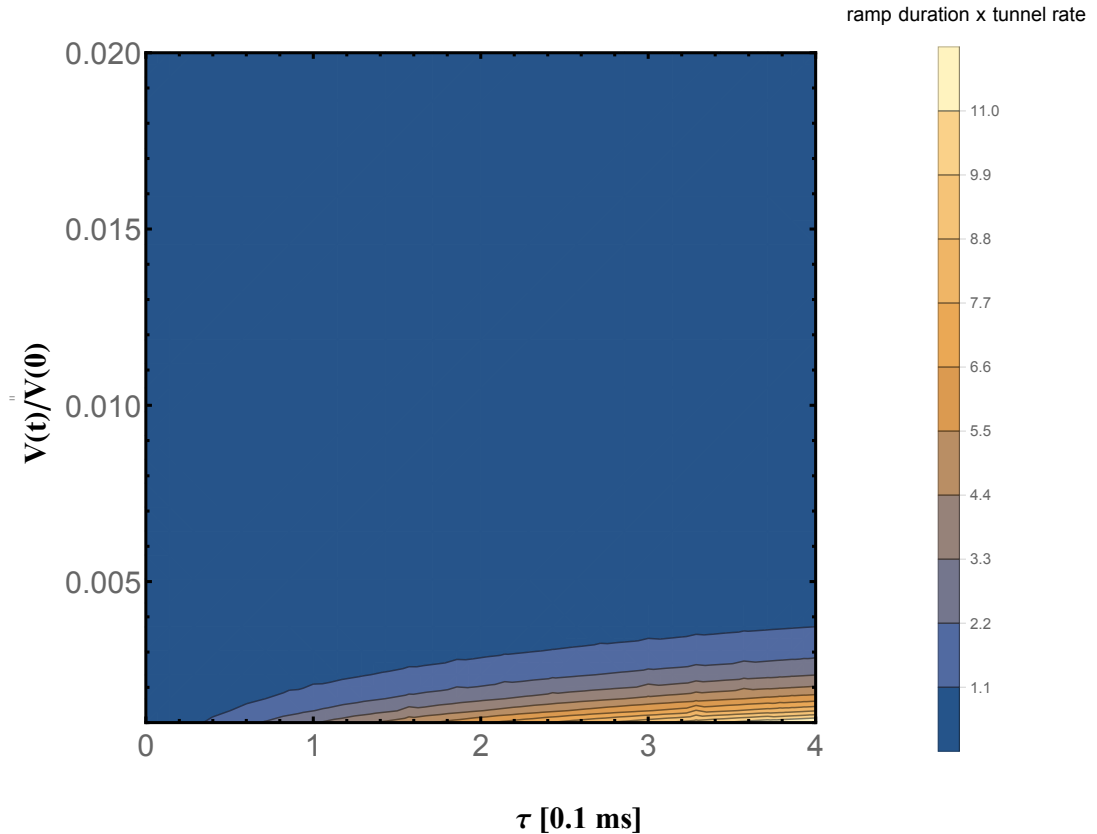
Figure 4.12: Tunnel rate times ramp duration depending on τ and V_{fin}.

The effect of tunnelling becomes apparent in the range expected, for longer characteristic ramp durations τ and small V_{fin}. This is due to atoms having more time before release to occupy neighbouring lattice sites.

Intensity noise sensitivity Displaced from the center by 12 lattice sites the simulation in Fig. 4.11 shows that over a rather broad range, τ and V_{fin} can be chosen such that a final std of 1.6 lattice sites is achieved. Concerning robustness the stabilised beam power fluctuate no more than 10 % on average. This would lead to a relative deviation of about 10 % in V_{fin} due to being linearly dependent on the beam power of the HDT beams following equation 2.1. Power fluctuations of 10 % will lead to relative trap frequency variations in the order of 5 %. At least in the harmonic regime the natural units of τ is the trapping frequency of the lattice[38], so one can expect variations in the optimal τ regime of around 5 % relative deviation. Such fluctuations will not result in a much larger spread in case of the HDT2, 12 lattice sites displaced case.

Compression along the horizontal plane Optimising the ramp along one dimension doesn't mean that all other horizontal directions will have their optimum in the same parameter regime. Adiabaticity and tunnelling have been observed in the previous section to affect the std of the final atomic probability distribution. The up to now neglected recapture procedure consisting of the mirrored ramp down at a faster time $\tilde{\tau}$ will introduce differences in the compression efficiency between different horizontal compression directions.
Concerning the ramping of the HDT beam the parameters chosen for the HDT2

compression won't necessarily be optimal in the other directions even if adiabaticity may not be an issue.
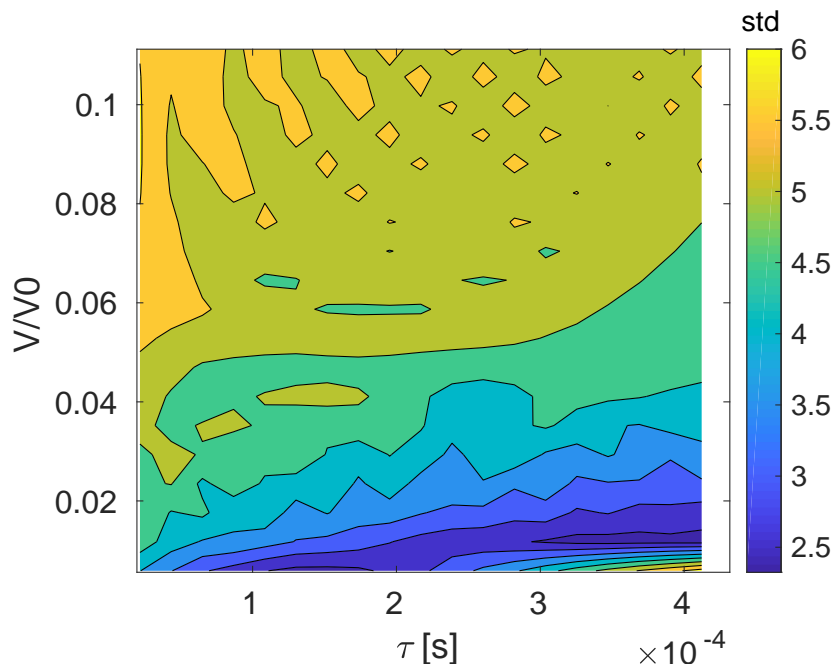

Figure 4.13: Simulated broadening during ramp down , release and recapture for the same parameter range as in Fig.4.11, along the fastest horizontal axis. Clear differences can be observed compared to the parameter landscape of the slow axis in Fig. 4.11.

The reason for the strong dependency on which axis the atom is initialised, leading to differences between the slow axis in Fig. 4.11 and the fast axis in Fig. 4.1,3 stems from the fact that the rising time is critical in this case. The ramp up consists of the same sequence as the ramp down mirrored. The deciding factor leading to difference is the fact that the ramp up heats atoms not only if performed very fast with respect time scale of the wave packets free propagation. But also depending on how steep the lattice potential is. The faster axis has a larger trapping frequency leading to a steeper parabola shape of a single lattice site in the harmonic approximation. Ramping up as fast as in the slow axis direction may heat up atoms in the fast axis enough to not be confined within a few lattice cites around the center. The ramp up in the optimal ramp chosen from Fig. 4.11 was performed by doubling $\tau_{up} = 2\tau_{down}$.

This is the reason why in Fig. 4.11 compression is rather good for larger τ and smaller Vfin. The total ramp down time is related to $\frac{\tau}{\sqrt{Vfin}}$. The larger τ and the smaller Vfin is, the longer the whole ramp down and release. And the slower the ramp down time, the slower the ramp up time due to the constant factor scaling τ_{down} and τ_{up}. For slow ramp downs the heating effect would be reduced and the std improved.

For the experiment that means compressing over the whole plane requires two ramps applied after each other with cooling in-between **and** along different horizontal axes.

4.5   Nonlinearity of the Gaussian potential

The last issue to address, is the question how well a ramp performs which is optimised for an atom close to the center for atoms further displaced. The limitation here arises due to anharmonicities at larger initial distances . , see section 4.3.2.
In order to compress atoms further away from the center at least two ramps will be again required. The second could be chosen based on Fig. 4.11 as atoms compressed after the first time and cooled should be in the vicinity of at least 12 lattice sites around the center. For choosing the first ramp an atom displaced by 40 lattice sites was used for determining the parameter land scape in Fig. 4.14 :
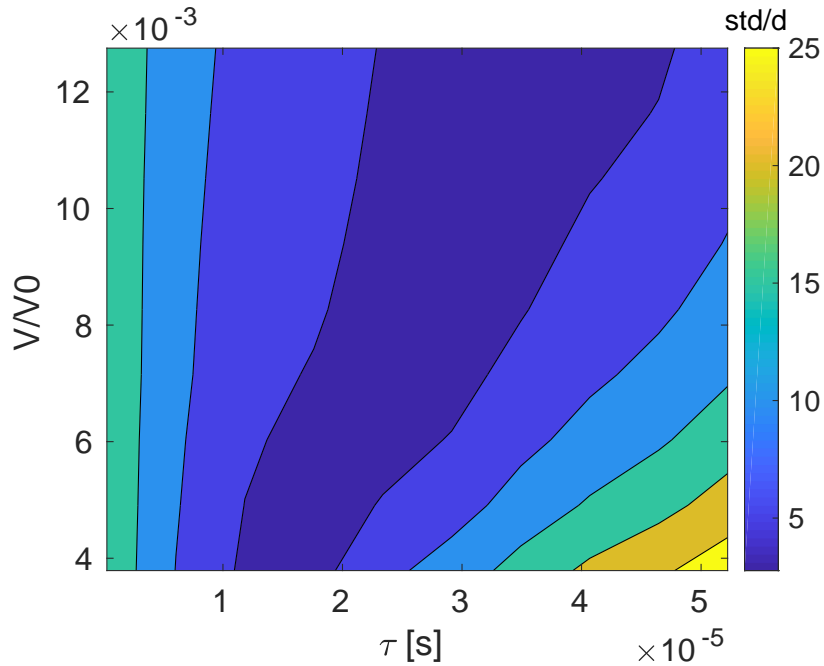

Figure 4.14: Simulated broadening during ramp down, release and recapture for an initial starting position of 40 lattice sites away from the center.

The deviation arises here from the effect of tunnelling being not enhanced in the same fashion as in the harmonic regime due to the flattening out of the Gaussian potential. This allows going for even lower V_{fin}.
The expected compression using the matrix multiplication of the ramp evolution predicts for atoms 40 lattice sites away a std of about 6.5 lattice sites. For a whole ensemble of atoms an idea of the entire compressed density may be gained by plotting the matrix values and overlapping them for all initial positions :
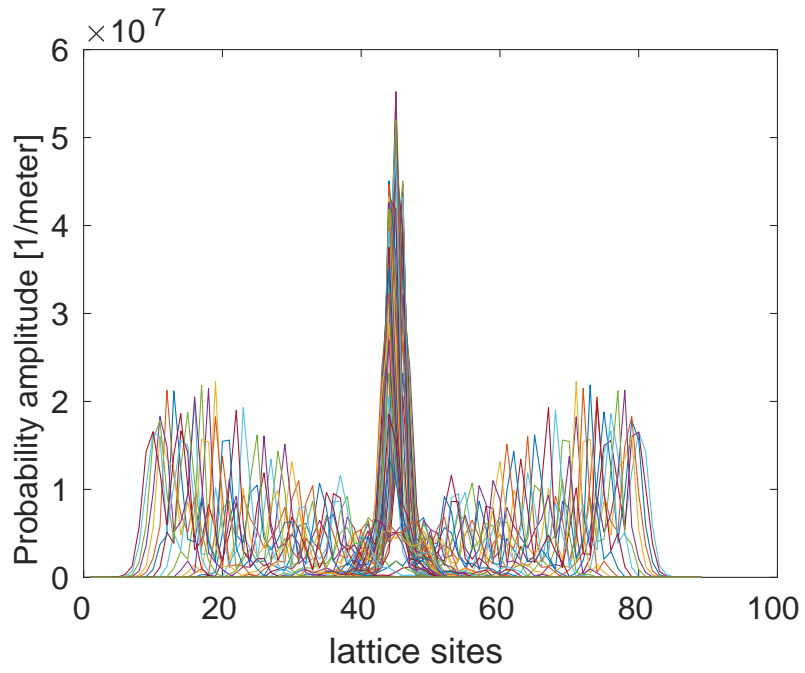
Figure 4.15: Overlap of final atomic distributions of independent simulation runs for ± 40 lattice sites inital displacement from the center. Optimal parameters following Fig. 4.11 and achieving a std of about 20 lattice sites .
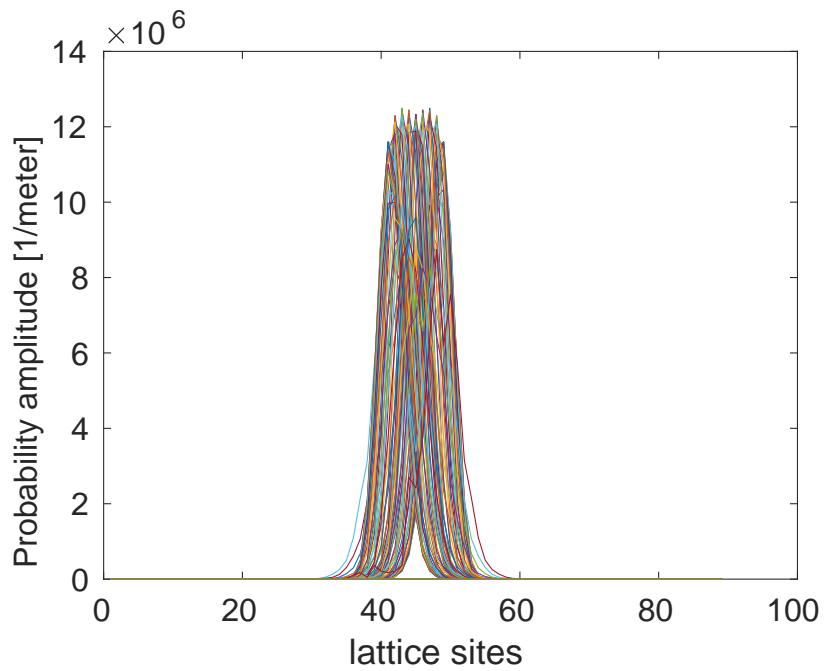

Figure 4.16: Plotted atomic distribution for all initial positions overlapped after applying the optimal ramp from Fig. 4.14. The longer duration τ compared to Fig. 4.15 is enough for atoms in the nonharmonic outer edge to travel into the harmonic region despite not perfectly fulfilling the quarter period condition.
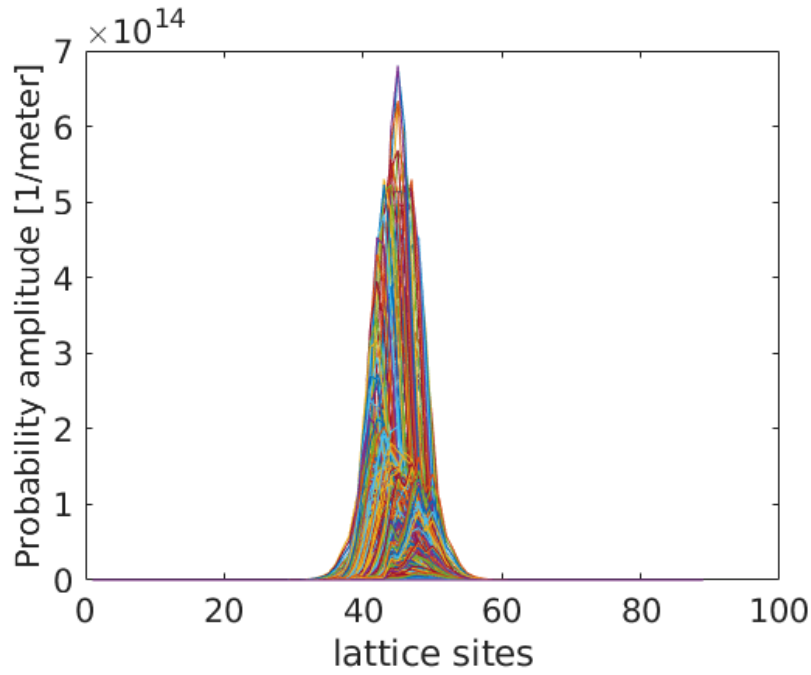
Figure 4.17: Plotted atomic distribution for all initial positions after ramp sequence overlapped. First applying the optimal ramp from Fig. 4.14 followed by the optimal ramp from Fig. 4.11 was performed. The std is 6 lattice sites, achieving the requirements for the plane selection procedure.

For the z axis compression all the above has been repeated and the following parameter plots for the first (ramp for long displacements of 20 lattice sites) and second ramp (for 8 lattice site displacements) have been calculated:
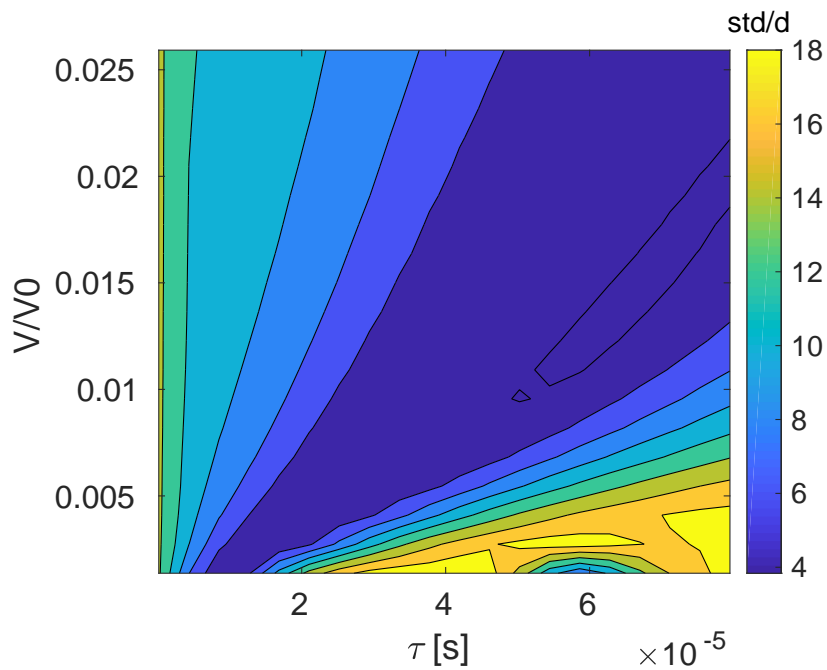

Figure 4.18: Simulated broadening during ramp down, release and recapture along the vertical direction for initial displacement of 25 lattice sites.
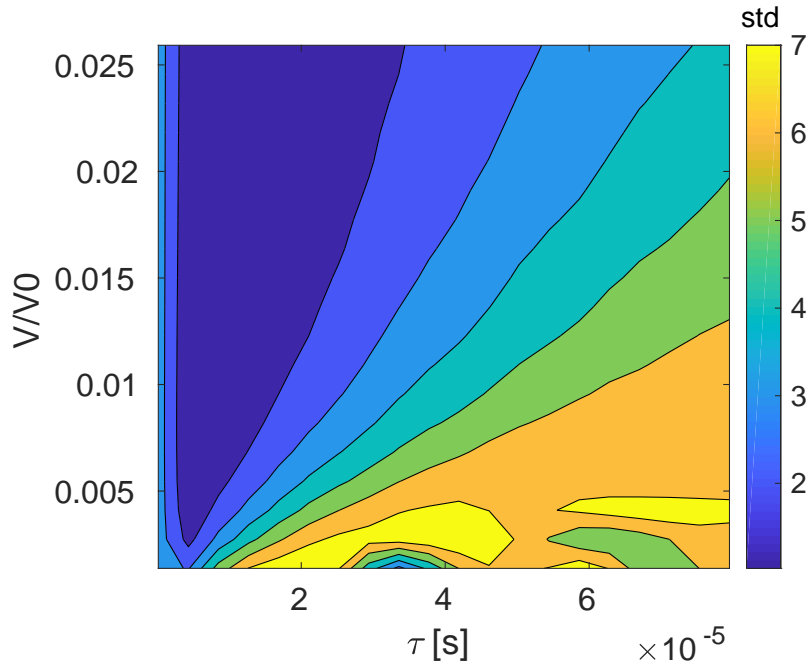
Figure 4.19: Simulated broadening during ramp down, release and recapture along the vertical direction for initial displacement of 8 lattice sites.

The difference in the vertical compression and the horizontal one lies in the much shallower Gaussian potential of the HDT beams in this case compared to the Gaussian VDT potential. This leads to less enhancement of directed tunnelling towards the center. Due to that a lower V_{fin} may be achieved than in the HDT compression. In addition the trapping frequency of the VDT lattice potential is high such that broadening during the ramp down and release are real constrictions along this direction.

The longest ramp duration would be the optimal ramp for vertical compression taking in total about 20 ms, therefore staying well within the time scale required.
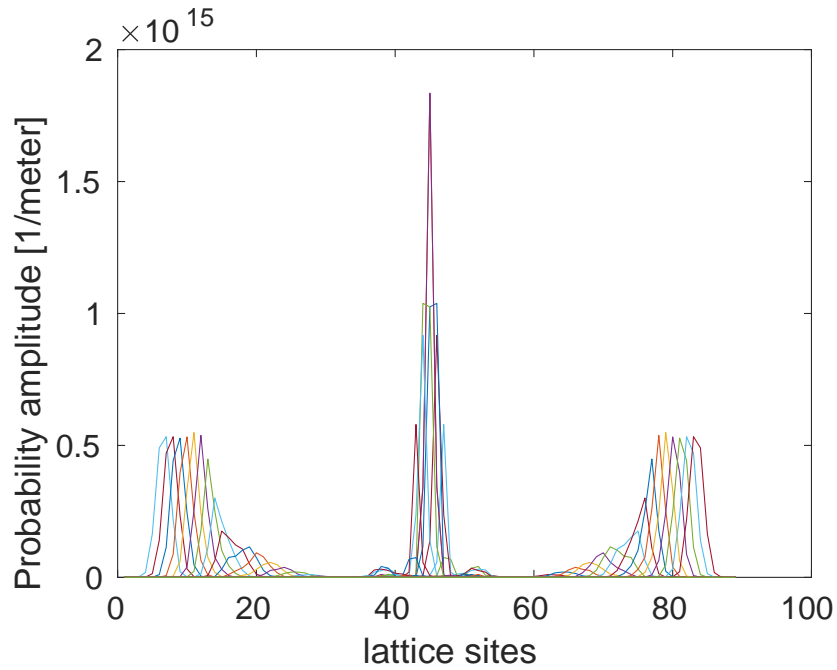
Figure 4.20: Simulated broadening during ramp down, release and recapture along the vertical direction. From ±40 lattice site displaced final distributions overlapped for two optimal compression ramps. std = 3 lattice sites. Considering only the inner 30 lattice sites for the std. The outer atomic distributions are less critical due to being exponential suppressed if arising from the 1/e radius of the MOT of about 50 µm.

4.6 Experimental implementation of the compression

The initial attempt in compressing atoms was taken only with a single ramp and while applying Molasses cooling .

(a) Before compression.

(b) After compression.
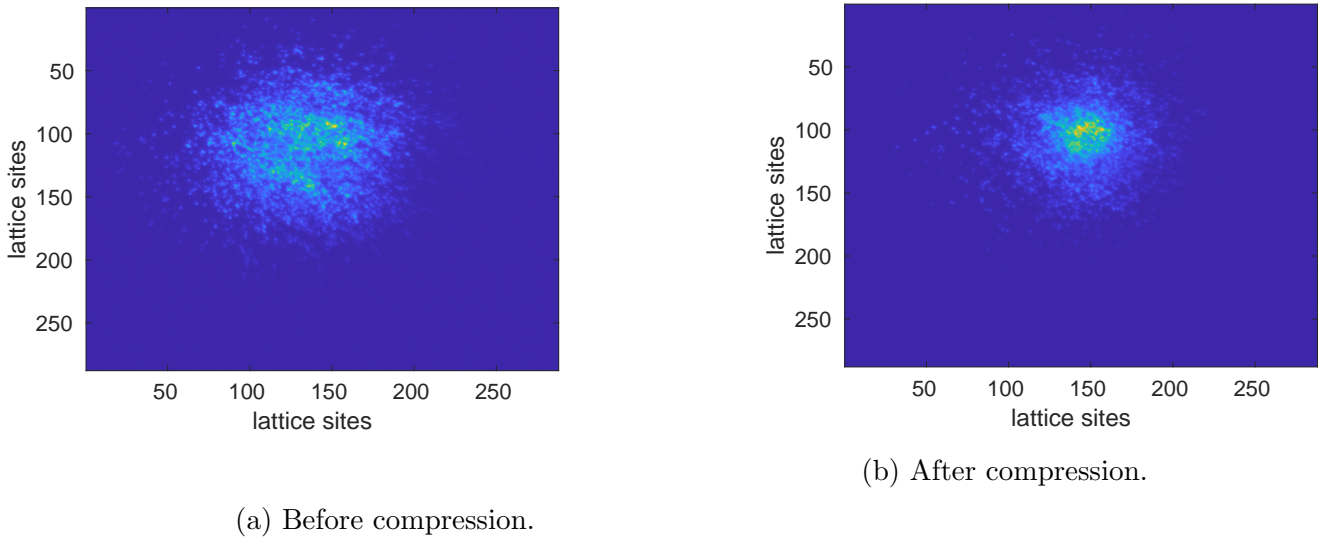
Figure 4.21: Fluorescence image of the atomic ensemble arising due to Molasses cooling off-resonantly exciting the atoms. The image was taken by the high NA objective. It was taken while zooming out, so not using the full NA. This can be seen by observing the extend of the field of view being much larger than assumed in the beginning of the chapter. The images were generated by adding 30 separate images.

The achieved compression is already clearly visible by eye. Observing the radial relative intensity distribution away from the calculated center of mass shows in Fig. 4.22 that the initial atomic distribution wasn't within the center of the trap. But nevertheless applying an intensity ramp optimised for only 12 lattice sites displacement already resulting in a reduction of the full width at half maximum (FWHM) by 20 lattice sites.
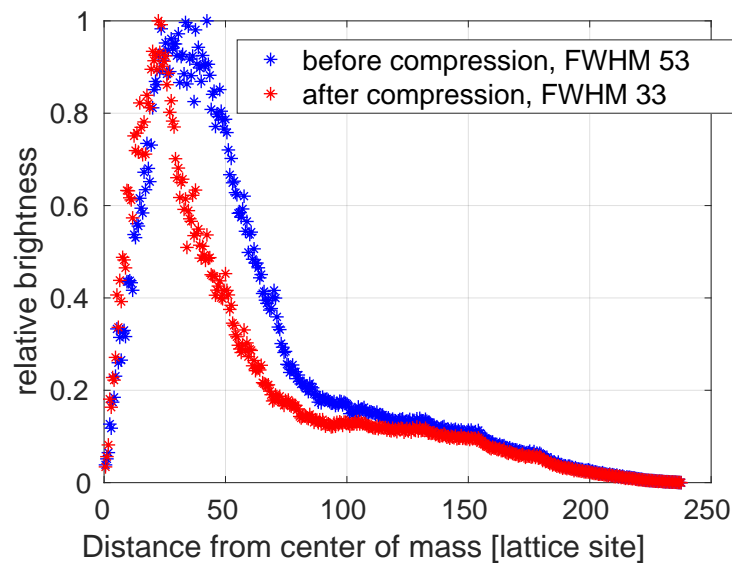

Figure 4.22: Radial distances from the center of mass measured by the brightness of each position before and after applying a single compression ramp.

Ground state cooling and multiple sequences would be promising improvement to try out experimentally. The fact that the achieved compression is surprisingly more efficient than conservatively estimated by simulation promises even better performance using the mentioned improvement than simulated.

5 CONCLUSION

5.1 Summary of results

5.1.1 Intensity stabilisation

Shot noise limited intensity stabilisation was achieved in a frequency range in which the atoms are especially sensitive to decoherence arising from intensity noise in a test setup. This was accomplished by an in-house developed, shot noise limited photodiodes optimised for the digital intensity stabilisation of the DQSIM experiment. It was possible to overcome the read-out noise limited loss of resolution of the digital control unit with it .

5.1.2 Compression of atomic ensembles in a 3D optical lattice

Compression of atoms confined within the 3 D optical lattice can be achieved in all spatial directions while applying successive compression intensity ramps and ground state cooling. For ensembles of atoms ranging from the entire field of view two compressions may achieve spatial atomic distributions with standard deviation of around 5 lattice sites around the center.

5.2 Outlook

The 5 photodiodes for the five lattice beams involved need to be installed within the experiment as soon as it is running again to quantify the achievable noise suppression in the main setup. From the RIN the gain in coherence time may be estimated and can be cross checked employing atomic interferometry.
The realisation of it allows the exclusion of intensity noise as a possible source of decoherence limiting the experiment.
The efficiency of the simulated compression ramps needs to be verified experimentally in order to move forward to single plane selection. The compression achieved in simulations along all direction promises an efficient atomic compression after a plane selection procedure. After ensuring the required magnetic field stability, addressing a limited volume of planes with a microwave pulse and push-out beam would be the next step forward for the experiment.

6 ACKNOWLEDGEMENTS

A CONTROL THEORY RECAP

A.0.1 Feedback system

There are in principle three ways to reduce the detrimental heating and decoherence effects intensity fluctuations can have for our quantum walk experiment. The most simple is to remove the origin of the fluctuations. The more involved way is to correct for such processes on the atoms after monitoring them by quantum error correction protocols as developed in [44], described in [43, pp.428-430] and applied for example experimentally in [45]. But non-unitary interactions with the environment cannot be cancelled out by unitary interactions preferably used by the experimenter like coherent microwave pulses. So over intermediate times the artificially enhanced stability will degrade.
The most direct way is to reduce the noise coupling into the system from the environment.
The suppression of laser intensity fluctuations can be achieved by applying control theory which will be reviewed in the following to introduce necessary concepts for the electronic design and the experimental characterisation.
A **feedback loop** is a system where the output is being compared with the value desired, the so called **setpoint**. The difference between the two or **error signal** is send to a control system and the control system is going to create a correction signal based on the error signal and inject it into the input again in order to minimise the error signal.
The process of closing a loop by feeding back a part of the output into the input leads to the alternative naming of **closed-loop system**.
The advantage to an open-loop approach is that unknown disturbances are compensated and no need for recalibration may arise over time. Downsides are that depending on the nature of the feedback and the control parameter choice stability issues may arise for certain signal frequencies and that rechecking output against setpoint to adjust the system slows down the whole system and decreases therefore always the bandwidth to some extent. Control theory assigns a system described by linear, time-invariant differential equations a transfer function relating input $x(t)$ and output $y(t)$. It is convenient to formulate the linear processes not only with real functions $q(t)$ in the time domain but also in terms of their Laplace transforms $\mathcal{L}[q(t)](s)$ as a function of $s = \sigma + i\omega$, $\sigma, \omega \in \mathbb{R}$. This allows the introduction of the transfer function in the s-domain, $G(s)$ under the assumptions that $x(t = 0) = y(0) = 0$ holds.

$$\sum_{j=0}^{n} \alpha_j y^{(j)}(t) = \sum_{j=0}^{m} \beta_j x^{(j)}(t)$$

$$\mathcal{L}[q(t)] = Q(s) = \int_0^\infty q(t)\exp(-st)\mathrm{d}t \tag{A.1}$$

$$G(s) = \frac{Y(s)}{X(s)}$$

with $n, m, j \in \mathbb{N}^{+0}$. Adding feedback to the system results in :
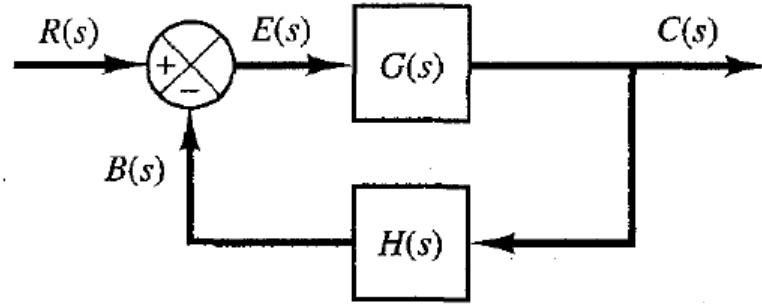
Figure A.1: Schematic introducing the terms (feedforward) transfer function $G(s)$, error signal $B(s)$, $H(s)$ the feedback transfer function , $C(s)$ the output at the branching point , $R(s)$ the set point signal and $E(s)$ the corrected input signal [46].

Without the input and output branching points the loop would be opened. That is the reason for calling $\frac{C(s)}{E(s)} = G(s)H(s)$ the open-loop transfer function.The closed-loop transfer function is $\frac{C(s)}{R(s)} = \frac{G(s)}{1+G(s)H(s)}$ using $C(s) = G(s)E(s) = G(s)(R(s) - B(s)) = G(s)(R(s) - H(s)C(s))$.

A.0.2 PID control

Concerning the input branching point in Fig. A.1, it could just calculate the difference between the feedback output and the set point to give an error signal. For a simple operational amplifier circuit this may already be enough to achieve higher stability and more linear behaviour at the cost of lower gain. But as electronically generated signals may need to be converted by an actuator into control actions in other applications and noise suppression in certain frequencies requires mores sophisticated adjustment of the error signal, the schematics needs to be generalised.
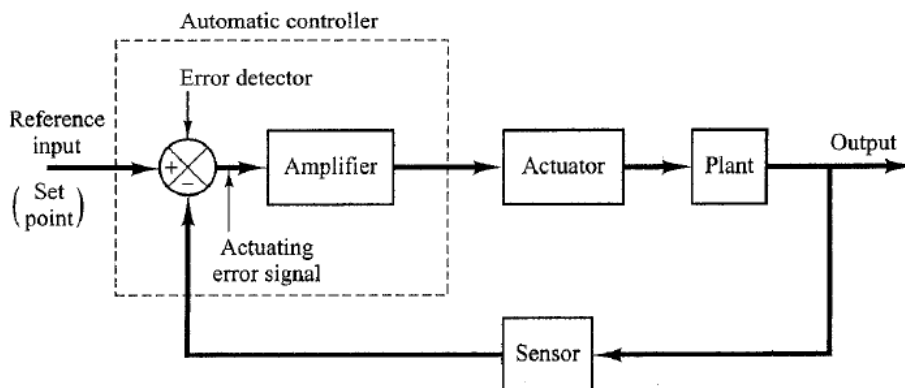
Figure A.2: Expanded feedback schematic. The error signal optimised by a specific amplification is send into the actuator converting it into a control action like a valve for example to affect the system or plant. Taken from [46].

To introduce the PID amplification scheme now: Let $e(t)$ be again the error signal and $u(t)$ the amplifier output. A proportional control action would generate an output proportional to the input $u(t) = K_p e(t)$, an integral control action an output

change rate proportional to the input $\dot{u}(t) = K_i e(t)$ and a differential an output proportional to the rate of change of the input $u(t) = K_d \dot{e}(t)$. The interpretation is that the differential control action approximates future corrections necessary by the present rate of change, the proportional one reacts to present changes and the integral one adjust the control action based on the accumulated past control actions. All combined one attains a Proportional-Integral-Derivative (PID) control action where each gain factor K_p, K_i andK_d is adjusted to accommodate the relevant time scales. Laplace transforming the combination results in

$$U(s) = (K_p + \frac{K_i}{s} + K_d s)E(s) \tag{A.2}$$

A.0.3 Analysing the control performance

time-domain picture Now assume a feedback system is set up and if present the PID gain parameters have some value to test the performance (possibly gained by following tuning rules like Ziegler and Nichols for example, see [25, p.33] or more generally explained in [50]). Modelling noise as a series of sudden disturbances a good input test function would be the step function θ.

$$\theta(t) = \begin{cases} 0 & \text{if} \quad t \leq 0 \\ 1 & \text{if} \quad t > 0 \end{cases} \tag{A.3}$$

But in principle any linear time-invariant system can be characterised by any non-trivial input function .

The most important criterion to judge a system is stability as this addresses the question if it can function in real applications or would in the worst case destroy itself in oscillations. For illustrative purposes only a brief overview of stability in the context of a second order system without feedback will be attempted like a damped harmonic oscillator or a low-pass filter of second order. The term order classifies transfer functions in the s-domain which can be represented as a fraction of polynomials and refers to the difference between the denominator polynomial order and the numerator order where the latter is always smaller for physical systems [46].

The so called standard second order transfer function is then as an open-loop transfer function $\frac{C(s)}{E(s)} = \frac{\omega_n^2}{\omega_n^2 + 2s\zeta\omega_n + s^2}$. When subjected to a step three different cases can be distinguished depending on the damping ζ.
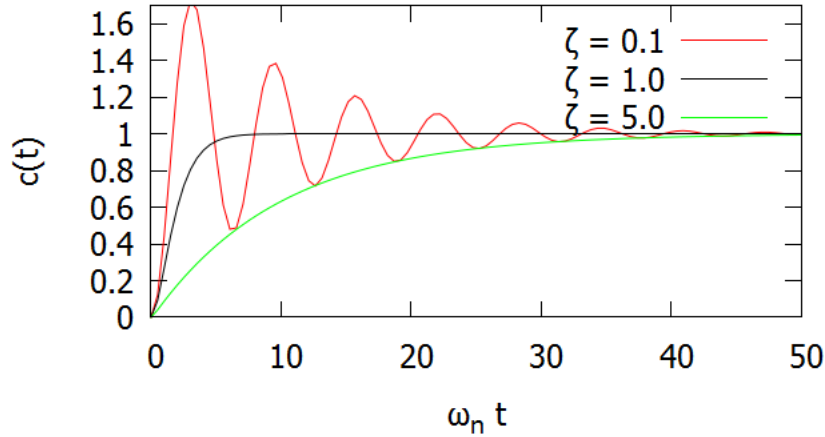
Figure A.3: Step responses of a standard second order system depending on damping factor ζ.

Overshoot (difference between maximum and steady state) and ringing become apparent for an underdamped configuration ($\zeta < 1$) and are signs for instability as they appear at the onsets of oscillation. The overdamped case is strongly slowed down in its **rising time** (time it takes to go from 10 % to 90 %). The smaller ζ the longer the **settling time** (time it takes to reach amplitude variations within 5 % of the steady state value. If oscillations would persist then there would be no steady state and the system is said to be **unstable**.

The poles of this transfer function are $\frac{s}{\omega_n} = -\zeta \pm \sqrt{\zeta^2 - 1}$. The oscillations would increase with time if ζ was negative and it is actually a general rule that a system is unstable if the poles of the transfer function lie on the right side of the s -plane. To generalise: A first order system always has the shape of an overdamped second order system. At higher orders it can be shown that the step response of a stable system is a combination of different first and second order responses weighted by the position of the respective poles in the complex plane [46].

Multiplying the PID control transfer function now to the feedforward transfer function allows to fine tune the way certain poles may contribute in the closed-loop transfer function for the overall transient behaviour of the step response in a versatile way.

s domain picture Another way of characterising the performance of a system is to look at the s-domain transfer function.

The transfer function may be obtained by Laplace transforming the step response derivative. The reason is that the Laplace transform of a step is $\Theta(s) = \frac{1}{s}$ so for a system with transfer function $G(s)$, $C(s) = G(s)\Theta(s)$ keeping in mind $\mathcal{L}[\dot{c}(t)] = C(s)/s = G(s)$.

Now it is possible to replace the s-domain description in the more intuitive frequency domain to some extent.

One may omit σ and substitute s by $i\omega$ for describing the steady state behaviour of the system for a sinusoidal input $x(t) = A\sin(\omega t)$ which can be proven for linear, stable, time invariant systems [46]. The transfer function $G(s)$ retains its shape then, so $y_{ss}(t) = G(i\omega)x(t)$. Steady state as in the sense of time t so large that exponential decay terms can be neglected as mentioned before. The same holds of

course then for all Fourier transformable or L^2 functions. A step function isn't included but its derivative luckily is so obtaining the transfer function in the frequency domain by Fourier transforming the derivative of a step response is an option.

Frequency domain analysis   The transfer function is a complex number for one frequency so a sinusoidal input results in a phase shifted and amplitude scaled sinusoidal output in this case.

Observing phase and amplitude shape of $G(i\omega)$ would then allow to optimise stability criteria against control bandwidth in the frequency domain.

In the case of the previous second order system substituting $s = i\omega$ the frequency transfer function $G(i\omega) = A(i\omega) \exp(i\alpha(i\omega))$ shows peaking in the transfer amplitude A occurring at frequency $\omega_r = \omega_n \sqrt{1 - \zeta^2}$ for $\zeta < \frac{1}{\sqrt{2}}$ of height $M_f = \frac{1}{2\zeta\sqrt{1-\zeta^2}}$.

This peaking is directly related to the overshoot height in the underdamped case $M_t = \exp(-\frac{\zeta}{\sqrt{1-\zeta^2}}\pi)$ and to the settling time $t_s = \frac{4}{\omega_n\zeta}$. If the phase α turns to $180°$ the amplitude has to be below 1 to avoid amplifying disturbances under a feedback sign change and enter instability. This motivates the definition of the phase margin $\gamma = -180° + \alpha(\omega_{cr})$ with ω_{cr} the frequency at which the amplitude equals 1. A phase margin of about 60 % is usually a good distance from instability as a rule of thumb. γ here is a function only of ζ and at $\zeta = 0.1$ the margin is $0.1°$ while at $\zeta = 1$ it is $67°$.

After the amplitude peaking a 1/frequency like roll-off sets in. The point where the amplitude drops below 3 dB from the DC gain indicates the 3-dB bandwidth and is here for $\zeta = 0.1$ at $1.5\,\omega_n$.
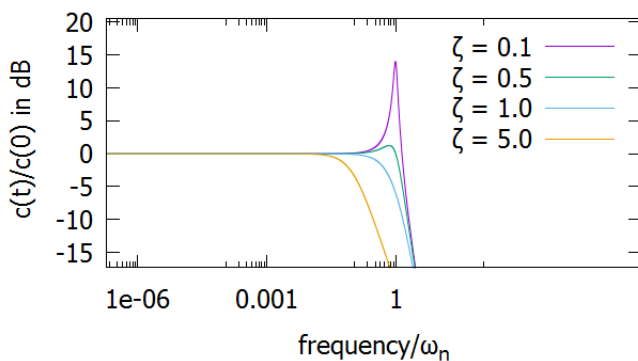
(a) The standard second order system frequency transfer amplitude for different dampings. Gain peaking height and bandwidth are counteracting each other.
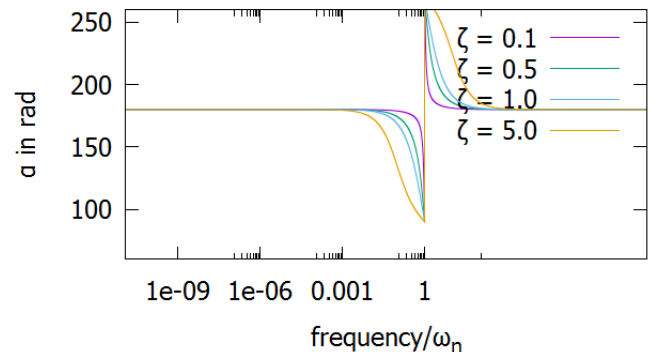
(b) The standard second order system frequency transfer phases for different dampings. No poles on the right side of the s plane and no phase close to zero agree in the stability analysis. Note the phase moving towards sign change in the same frequency range of the gain roll-off.

In general systems frequency response and transient behaviour are valid and complete ways of characterising a system and each domains characteristics are connected like in this example .

B   NOISE REDUCTION MEASURES

B.1   Noise types overview

Following [65, pp.236-240] noise can be classified by observing the frequency domain it originates. Modes at around 1 Hz can be swinging modes of a building or turbulent air flows. From 1 Hz to 100 kHz noise could come from mechanical resonances like foot steps, air conditioning or pumps. 50 Hz line hums can also magnetically couple into devices making smd versions due to being more compact also more robust in not picking up such noise excessively. This is also one of the reasons why the final Pd was mostly designed with smd resistors and capacitors. The other being the handiness of a smaller sized device on an optical table. Ground loops will lead to 50 Hz and harmonics on voltage signals too. And if the electronics is exposed to ceiling light, normal diodes can exhibits 50 Hz and harmonics due to the 50 Hz modulation of the ceiling light being converted to 50 Hz current noise by the photoelectric effect.
EMI can be coupled from computers who tend to radiate sizeable amounts into the environment and usually in frequencies above 100 kHz. Around this frequency switching power supplies also contribute noise peaks due to their transformer action.

B.2   Additional Intrinsic noise

Dropping one of the assumptions in section 3.4.2, now additional resistor noise will be considered. Depending on the design of the resistor and its constituent material an 1/f like noise structure may appear depending on the voltage drop over the resistor. Potentiometer such as the one to tune the internal compensation voltage for the second state of the photodiode design exhibit such noise. That necessitated $1000\,\mu F$ capacitor after the potentiometer to filter out the low frequency excess noise.
Similarly lower quality resistors such as carbon film and thick film or even thin film smd resistors show this excess noise [17] [66]. In the case of carbon film, it arises from imperfect contacts of the granules of carbon [49, p.60]. Many characterising measurements have been taken for this type of noise, for example in the context of high sensitivity applications for gravitational wave detection [62].

B.3   EMI shielding

Now to drop the assumption of a quite environment, suppression schemes of EMI will be shortly reviewed. In principle electromagnetic radiation couples mostly into supply lines. Direct coupling through the shielding of the the die-cast aluminium boxes is unlikely due to its absorption and reflection losses radiated signals may experience when impinging on it (for steel and copper estimates see [64, p.219]) .
Common mode noise in the power supply lines can be suppressed by ferrites [64, p.239]. Ferrites of material N30 for example may be able to suppress well above 100 kHz range common mode disturbances.
Filtering capacitors to bypass noise to the box shielding before it reaches the PCB were also necessary to use. $0.1\,\mu F$ and $10\,\mu F$ tantalum proved reliable in avoiding

not only lower but also higher frequency noise from noisy supplies reaching the circuit, acting like commercially available suppression capacitors. The two ground problem generating ground loops with 50 Hz fluctuations was circumvented by not grounding the PD box with the common grounded optical table using plastic posts to place it. In addition breaking the ground connection of the power supply using diode protected power chords developed in [26] were of use.

C TIME DEPENDENT SCHRÖDINGER EQUATION

Modelling for the compression scheme the dynamics of the atom in the optical lattice classically is insufficient. A classical simulation with point particle like atoms does not take into consideration heating within the lattice sites for example. It was used to get a first idea about the effect of anharmonicity though which was illustrated by the movement of a classical particle in a Gaussian potential calculated by the Runge- Kutta method [74, pp.710-722] in Fig.C.1.
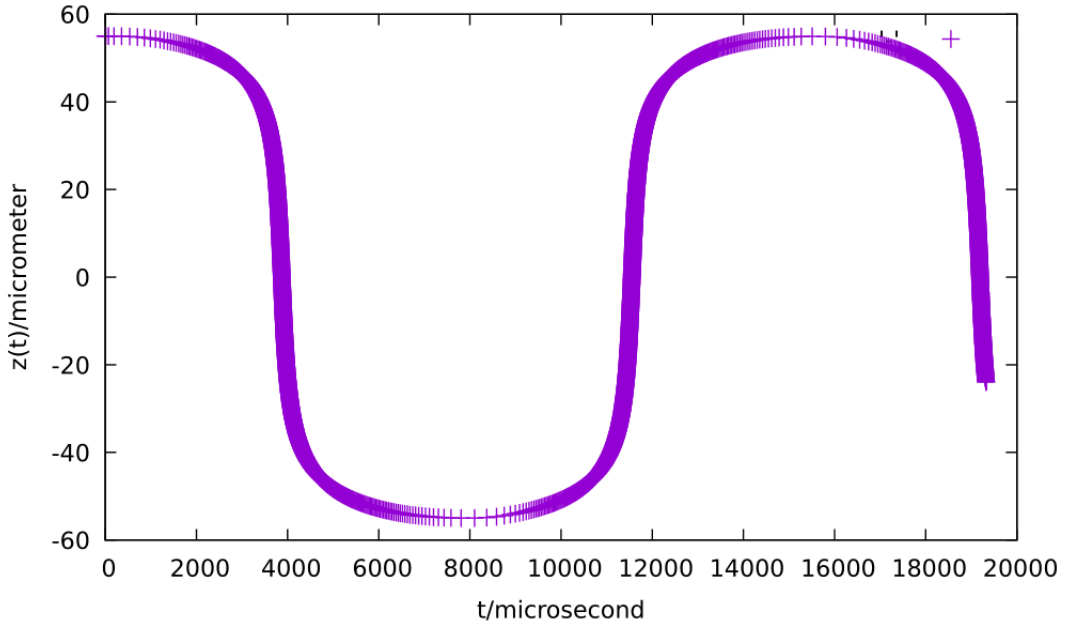

Figure C.1: Simulated trajectory of a classical atom within a Gaussian potential.

Therefore a quantum mechanical treatment of the ramping is required at least concerning the atoms. The lattice Hamiltonian during the ramp for the compression scheme is time dependent and for numerically solving the time dependent Schrödinger equation the so called split step operator method was chosen and further refined using the Richardson interpolation following [39, pp.1135-1140] for both. In both cases, classically and quantum mechanically, one needs to discretise time and space. So at the end a measure for the correctness of the numerical result in dependence of the grid sizes will be presented.

C.1 Split-step operator method

Starting with an initially known wave function the time evolution operator is applied to it in successive steps assuming a Hamiltonian of the form

$$\hat{H}(x,t) = \hat{T} + \hat{V} = \frac{\hat{p}^2}{2m} + V(x,t) \qquad (\text{C.1})$$

One needs to split the time evolution operator to take advantage of the fact that the kinetic operator is just a factor in momentum representation of the wave function. In contrast the potential operator is a factor in position representation . Switching

between the two domains can be accomplished by the numerically efficient Fast Fourier Transform (FFT) algorithm. That way, each separate time evolution operator can be computed in the most efficient representation of the wave function for it .

Using the midpoint approximation for a Riemann integral for calculating the contribution of the time dependent part of the time evolution operator yields

$$U(t, t + \Delta t) = \exp(-\frac{i}{\hbar} \int_t^{t+\Delta t} dt' H(x, t')) = \exp(-\frac{i}{\hbar}(\Delta t \frac{p^2}{2m} + \int_t^{t+\Delta t} dt' V(x, t')))$$

$$= \exp(-\frac{i}{\hbar}(\Delta t \frac{p^2}{2m} + V(x, t + \Delta t/2))\Delta t + O(\Delta t^3))))$$

(C.2)

With the following splitting, derived using the Baker-Campbell-Hausdorff (BCH) relations for an operator of the form of $H = H_1 + H_2$ and $\delta = \frac{\Delta t}{\hbar}$, one attains :

$$\exp(-iH\delta) = \exp(-iH_2\delta/2) \exp(-iH_1\delta) \exp(-iH_2\delta/2) + O(\delta^3) \qquad \text{(C.3)}$$

This can be used to arrive at the following representation of the time evolution operator of

$$U(t, t + \Delta t) = \exp(-iV(x, t + \Delta t/2)\frac{\Delta t}{2\hbar}) \exp(-i\frac{\Delta t}{\hbar}\frac{p^2}{2m}) \exp(-iV(x, t + \Delta t/2)\frac{\Delta t}{2\hbar}) + O(\Delta t^3)$$

(C.4)

The accuracy has to be understood as a local error, so as the error made in a single step. It can be proven and was already used in equation C.4 that this error from the BCH relations estimate even holds if each decomposed operator is only calculated in the order of $O(\Delta t^3)$ as is the case with the time dependent potential term.

The number of steps is usually in the order of $\frac{1}{\Delta t}$. Then over a full simulation with successive steps applied to the wave function the overall accuracy or global error is of the order of $O(\Delta t^2)$. Therefore the split step will be called a second order method, referring to the global error scaling.
The split-step method is also known as Strang splitting and originates from [68].

C.2   Richardson Interpolation

A method of higher order would result in larger possible step sizes one can choose and this in turn in less computation time.
One way to achieve this is just using more split terms. Another way to go is following the proposal in [69]. There it is suggested to calculate the time evolution of each step in different time step sizes. Then they are linear combined such as to cancel out the lower order error terms.
When Taylor expanding the final wave function calculated in terms of Δt only even orders of Δt contribute. This is due to when writing out the local expansion in terms of the BCH relatins of the operators only odd orders don't cancel out with

higher expansion terms.[67, p.335]. And the global error scaling is an order smaller. So this leads to :

$$\psi_{\Delta t}(x, t_{end}) = a\Delta t^2 + b\Delta t^4 + c\Delta t^6 + ... \quad , \tag{C.5}$$

with a, b, c some real coefficients. It follows thus that arbitrarily higher even order schemes cam be constructed based on the split-step method .

For example to achieve a sixth order global error method from the Strang splitting used in the previous section one repeatedly computes the final wave function in step sizes of Δt , $\Delta t/2$ and $\Delta t/3$ and combine those results in each step such that :

$$\psi_{\Delta t^6}(x) = -\frac{13}{24}\psi_{\Delta t} + \frac{32}{3}\psi_{\Delta t/2} - \frac{81}{8}\psi_{\Delta t/3} \tag{C.6}$$

where the coefficients of this linear combination result from explicitly writing down the Taylor expansion and solving the resulting linear set of equations [39, p.1139]. Unlike the original Strang splitting, using the Richardson interpolation the norm of the wave function is not preserved. This is due to breaking the unitarity of the overall time evolution in each step. This can be exploited to attain a measure of accuracy even if the solution isn't analytically known by observing the norm. This can be illustrated by the following check of the scaling behaviour of error against time spacing Δt for an harmonic oscillator potential :
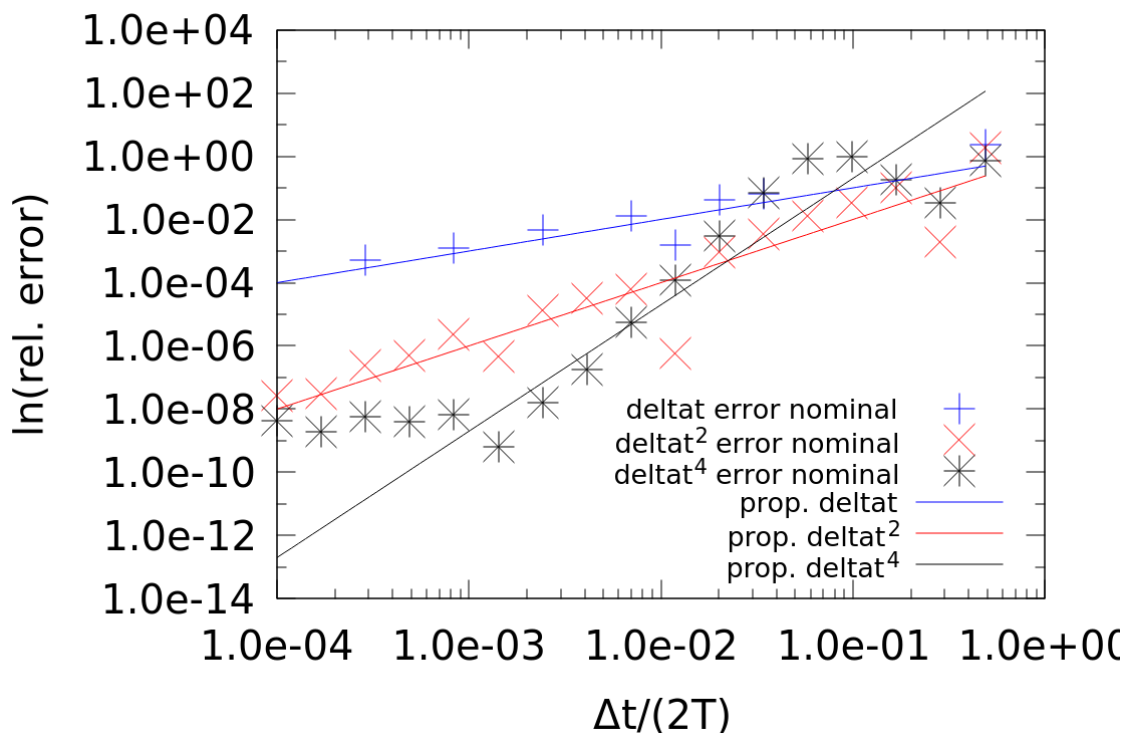
Figure C.2: logarithmic deviation of the norm 1 against the step size Δt in units of 2 harmonic oscillator periods for the second, fourth and sixth order global error method. At smaller step sizes higher order methods are limited not by the accuracy of the method but by rounding errors. At larger step sizes the coefficients of the Richardson interpolation aren't accurate as the Taylor expansion does not hold then well.

The exact same plot can be achieved by substituting the deviation from the norm by energy difference between the known harmonic oscillator and the numerical simulation .

70

The observation of the norm will be thus used to monitor the correctness of the simulation with the unknown wave functions arising during compression.

As a side note: Details concerning the limitations on the differential equations for which the Richardson interpolation is applicable may be taken from [74, p.724]

D CIRCUIT LAYOUT
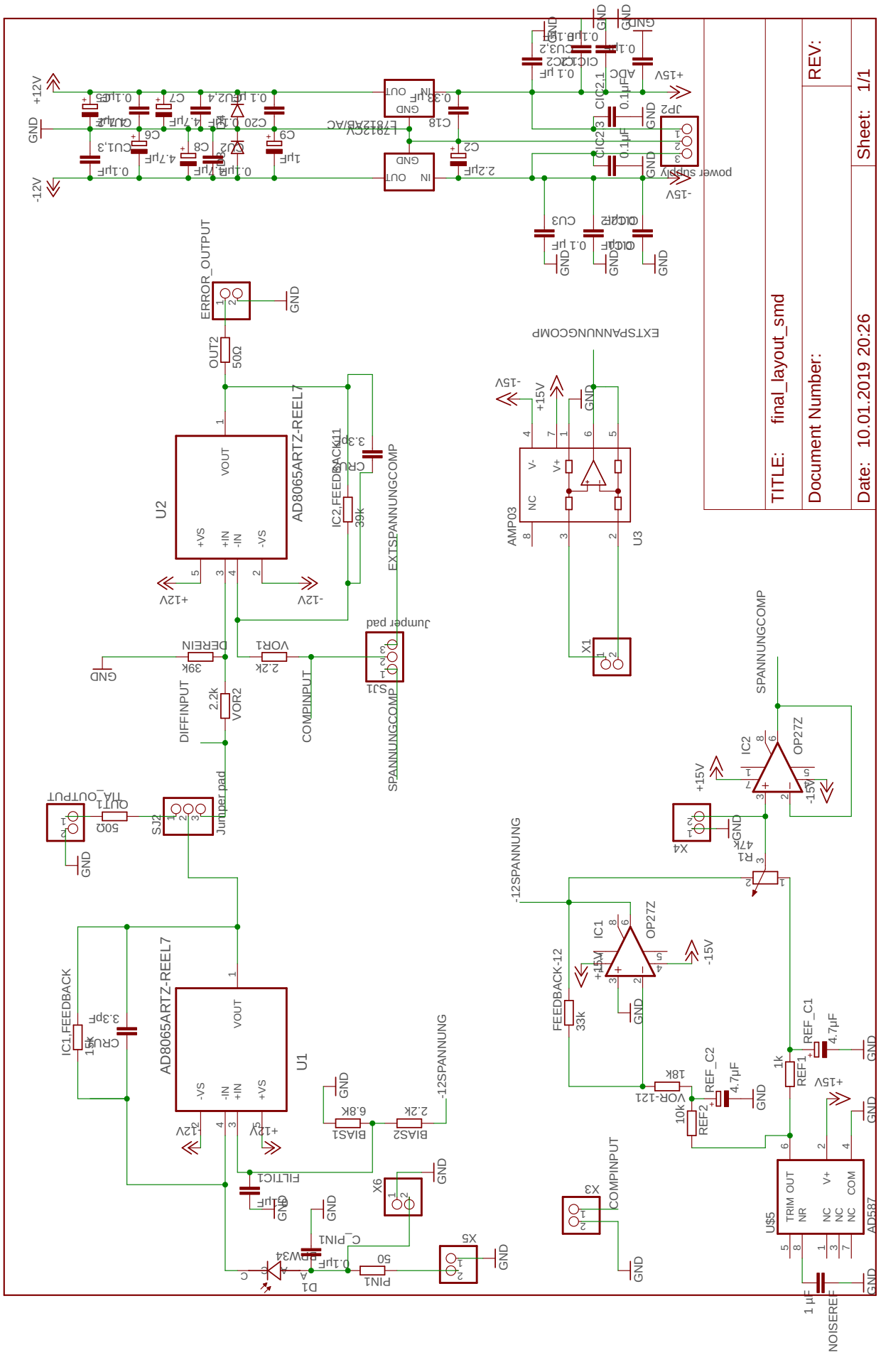
Figure D.1: Schematics of the photodiode amplifier.

73

29.03.2019 03:16 C:\Users\llugano71\Desktop\final_layout_smd.sch (Sheet: 1/1)

Figure D.2: PCB layout. Length units in mm.

29.03.2019 03:23 f=2.80 C:\Users\lugano71\Desktop\final_layout_smd_2.brd

E BIBLIOGRAPHY

[1] N. Gisin, G. Ribordy, W. Tittel, , H. Zbinden,
Quantum cryptography,
Rev. Mod. Phys. 74, 145 , March 2002

[2] Peter W. Shor,
Polynomial-Time Algorithms for Prime Factorization and Discrete Logarithms on a Quantum Computer,

Siam J. Comput., Volume 26, Issue 26, 1484–1509, 1997

[3] S. E. Venegas-Andraca,
Quantum walks: a comprehensive review Quantum Information Processing,
Volume 11, Issue 5, pp 1015–1106, 2012

[4] M. Genske,
Electric Quantum Walks with individual atoms,
master thesis, University of Cologne, performed at University of Bonn, 2012

[5] M. Sajid, J. K. Asbóth,D. Meschede, R. Werner, A. Alberti1, *Creating Floquet Chern insulators with magnetic quantum walks,*
`https://arxiv.org/abs/1808.08923`, 2018

[6] A. Ahlbrecht, A. Alberti, D. Meschede, V. B. Scholz, A. H. Werner ,R. F. Werner
Molecular binding in interacting quantum walks,
New Journal of Physics, Volume 14, 2012

[7] S. Brakhane,
The Quantum Walk Microscope,
Phd thesis, University Bonn, 2016

[8] C. Robens,
Testing the Quantumness of Atom Trajectories, Phd thesis, University Bonn,
2016

[9] J. Zopes,
Sorting atoms in spin dependent optical lattice,
Master thesis, 2014,University of Bonn

[10] D. Döring,
Ein Experiment zum zustandsabhängigen Transport einzelner Atome, Diploma thesis, University Bonn, 2007

[11] M. Karski, L. Förster, J. Choi, A. Steffen, W. Alt, D. Meschede , A. Widera,
Quantum Walk in Position Space with Single Optically Trapped Atoms,
Science, 325(5937):174-177, 2009, ISSN 0036-8075

[12] T.W. Hänsch, A.L. Schawlow,
cooling of gases by laser radiation,
Optics Communication, Volume 13,1 , 1975

[13] E. L. Raab, M. Prentiss, A. Cable, S. Chu, D. E. Pritchard,
Trapping of Neutral Sodium Atoms with Radiation Pressure,
Phys. Rev. Lett. 59, 2631 , 1987

[14] *Threedimensional Viscous Confinement and Cooling of Atoms by Resonance Radiation Pressure*

[15] C.F. Roos,A. Alberti, D. Meschede, P. Hauke, H. Häffner,
Revealing quantum statistics with a pair of distant atoms,
Phys. Rev. Lett. 119, 160401, 2017

[16] W. Ketterle et al.,
Bose-Einstein Condensation in a Gas of Sodium Atoms,
Phys. Rev. Lett. 75, 3969 , 1995

[17] P. Hoowitz, W. Hill,
The Art of Electronics ,
Cambridge University Press,3rd Edition, 2015

[18] M. Karski et al ,
Imprinting patterns of neutral atoms in an optical lattice using magnetic resonance techniques,
New J. Phys. 12 065027, 2010

[19] Y. Band, Y. Avishai,
Quantum Mechanics with Applications to Nanotechnology and Information Science
first edition, Academic Press, 2012

[20] S. Kuhr, W. Alt, D. Schrader, I. Dotsenko, Y. Miroshnychenko, W. Rosenfeld, M. Khudaverdyan, V. Gomer, A. Rauschenbeutel, and D. Meschede,
Coherence Properties and Quantum State Transportation in an Optical Conveyor Belt ,
Phys. Rev. Lett. 91, 2003

[21] T. A. Savard, K. M. O'hara, and J. E. Thomas,
Laser-noise-induced heating in far-off resonance optical traps ,
Physical Review A, Volume 56, Number 2, August 1997 `https://physics.ncsu.edu/jet/publications/pdf/LaserNoise.pdf`.

[22] A. Alberti et al.,
Decoherence models for discrete-time quantum walks and their application to neutral atom experiments,
New Journal of Physics 16 12,3052,2014

[23] moglabs ARF/XRF device manual

[24] MATLAB R2017b , The MathWorks, Inc., Natick, Massachusetts, United States

[25] M. Werninghausen,
Controlling atom transport in a two-dimensional state-dependent optical lattice,
Master thesis, University of Bonn, 2017

[26] P. Du,
Optical Intensity Control Based on Digital and Analog Systems,
Master thesis, University of Bonn, 2018

[27] P.C.D. Hobbs,
Building Electrooptical Systems, making it all work,
second edition,Wiley, 2009

[28] D. Meschede,
Optik,Licht und Laser,
3. Edition,Vieweg+Teubner, 2008

[29] M. Gustavsson,
A quantum gas with tunable interactions in an optical lattice,
PhD thesis, University of Innsbruck

[30] Keysight M3300A PXIe Arbitrary Waveform Generator and Digitizer with Optional Real-Time Sequencing and FPGA Programming,
datasheet

[31] J. Graeme,
Photodiode Amplifiers, Op Amp solutions,
McGraw Hill Book, 1996

[32] datasheet bpw 34 osram

[33] datasheet ad8065 Analog devices

[34] F. Seifert,
Resistor Current Noise Measurements,
2009, `https://dcc.ligo.org/public/0002/T0900200/001/current_noise.pdf`

[35] S. Kuhr,W. Alt, D. Schrader, I. Dotsenko, Y. Miroshnychenko, A. Rauschenbeutel, and D.Meschede,
Analysis of dephasing mechanisms in a standing-wave dipole trap,
Phys. Rev. A 72, 02,3406, 2005

[36] G. J. A. Edge,R. Anderson,D. Jervis,D. C. McKay,,R. Day,S. Trotzky,and J. H. Thywissen,
Imaging and addressing of individual fermionic atoms in an optical lattice,
Phys. Rev. A92, 06,3406, 2015

[37] S. Kuhr,W. Alt, D. Schrader, I. Dotsenko, Y. Miroshnychenko, W.Rosenfeld, M. Khudaverdyan, V. Gomer, A. Rauschenbeutel, and D. Meschede,
Coherence Properties and Quantum State Transportation in an Optical Conveyor Belt,
Phys. Rev. Lett., 91,21,3002, 2003

[38] W. Alt,
Optical control of single neutral atoms,
dissertation, university of Bonn, 2004

[39] D. A. Steck,
Quantum and Atom Optics,
lecture notes,last revised version April 2018,
`http://atomoptics-nas.uoregon.edu/~dsteck/teaching/`
`quantum-optics/quantum-optics-notes.pdf`

[40] Les Houches,
Many-Body Physics with Ultracold Gases, Session XCIV, 28 June to 23 July 2010,
Oxford University Press,2013

[41] K. V. Krutitsky,
Ultracold bosons with short-range interaction in regular optical lattices,
`https://arxiv.org/pdf/1501.03125.pdf`

[42] V. Schilling ,
A Magnetic Elevator for Neutral Atoms into a 2D State-dependent Optical Lattice Experiment,
master thesis, 2015, University of Bonn

[43] S. Haroche, J. Raimond ,
Exploring the Quantum Atoms, Cavities and Photons,
Oxford University Press, 2006

[44] H. M. Wiseman,
Quantum theory of continuous feedback,
Phys. Rev. A 49, 2133 , 1994

[45] T.B. Pittman, B.C Jacobs, J.D. Franson,
Demonstration of Quantum Error Correction using Linear Optics,arxiv,2005,
`https://arxiv.org/abs/quant-ph/0502042`

[46] Katsuhiko Ogata ,
Modern Control Engineering,
Prentice Hall, 4th edition, (2001)

[47] J.C. Campbell et al.,
High-saturation-current InGaAs/InAlAs charge-compensated uni-traveling-carrier photodiode,
phys. stat. sol. (a) 201, No. 13, 3037–3041 (2004)

[48] J. Dostal,
Operational Amplifiers,
Butterworth-Heinemann,1993

[49] G. Vasilescu,
Electronic noise and interfering signals, principles and applications,
Springer,2005

[50] G. C. Goodwin, S. F. Graebe, M. E. Salgado,
Control System Design,
Prentice Hall, 2000

[51] T. Groh,
Fast transport of single atoms in optical lattices using quantum optimal control,
master thesis , University Bonn, 2018

[52] J. Bechhoefer,
Feedback for physicists: A tutorial essay on control,
Review of modern Physics, volume 77, 2005

[53] W. Zhou,
Robust Holographic Generation of Arbitrary Light Patterns: Method and Implementation,
master thesis, University of Bonn

[54] E. L. Hahn,
Spin echoes,
Physical Review 80.4 (1950) 580

[55] N. Thau,
Optimal quantum control of atomic wave packets in optical lattices,
PhD thesis , 2018,University of Bonn

[56] J. Foot,
Atomic Physics ,
Oxford University Press, 2005

[57] datasheet PDQ80 quadrature position detecting photodiode,
`https://www.thorlabs.com/drawings/381cce124c73dc01-23A53870-9F41-F624-EDD90058`
`PDQ80A-SpecSheet.pdf`

[58] V. Vuletic et al.,
Creation of a Bose-condensed gas of ^{87}Rb *by laser cooling*,
`https://arxiv.org/abs/1705.03421`

[59] M. E. Gehm, K. M. O'Hara, T. A. Savard, and J. E. Thomas,
Dynamics of noise-induced heating in atom traps,
Phys. Rev. A 58, 3914 , 1998

[60] G. Ramola,
A versatile digital frequency synthesizer for state-dependent transport of trapped neutral atoms,
master thesis, University of Bonn, 2015

[61] S. Mandt,
Transport and Non-Equilibrium Dynamics in Optical Lattices, from Expanding Atomic Clouds to Negative Absolute Temperatures,
PhD thesis, University of Cologne , 2012

[62] F. Seifert,
Resistor Current Noise Measurements,
2009, `https://dcc.ligo.org/public/0002/T0900200/001/current_noise.`
`pdf`

[63] S. Kuhr et al.
Analysis of dephasing mechanisms in a standing-wave dipole trap,
Phys. Rev. A 72, 023406, 2005

[64] P.J. Fish,
Electronic Noise and low noise design,
Macmillian New Electronics, 1993

[65] M. Weidemüller, C. Zimmermann,
Interactions in ultracold gases , from atoms to molecules,
Wiley VC-H,2003

[66] M. Belman, Y. Hernik,
Selecting Resistors for Pre-Amp, Amplifier, and Other High-End Audio Applic-
ations,
Vishay technologie technical note,
`https://www.eetimes.com/document.asp?doc_id=1278251`

[67] J. Yang,
Nonlinear Waves in Integrable and Nonintegrable Systems,
siam, mathematical Modelling and Computation, 2010

[68] G. Strang,
On the construction and comparison of difference schemes ,
Siam J. Numer. Anal. Vol. 5, No. 3, 1968

[69] H. Yoshida,
Construction of higher order symplectic integrators,
Phys. Lett. A Vol. 150, Issues 5–7, 1990, Pages 262-268

[70] M. Khudaverdyan,
Addressing of individual atoms in an optical dipole trap,
Diploma thesis, University of Bonn,2003

[71] L. Russella, R. Kumara, V. B. Tiwaria, S. Nic Chormaica,
Measurements on release-recapture of cold ^{85}Rb *atoms using an optical nanofibre*
in a magneto-optical trap,
`https://arxiv.org/pdf/1303.7344.pdf`

[72] E. Kochkina *stigmatic and Astigmatic Gaussian Beams in Fundamental Mode,*
PhD thesis, University of Hannover, 2013

[73] R. Grimm, M. Weidemüller,
Optical dipole traps for neutral atoms,
Advances in Atomic, Molecular and Optical Physics, Vol. 42 , 2000

[74] W. H. Press, S. A. Teukolsky, W. T. Vetterling, B. R. Flannery *Numerical*
Recipes in C,
Cambridge University Press, 2002

[75] M. Born, V. Fock,
Beweis des Adiabatensatzes,
Zeitschrift für Physik, Vol. 51, issue 3-4, pp. 165-180, 1928

[76] A. Messiah,
Quantum Mechanics, Volume 2,
North Holland Publish Company Amsterdam, 1962

[77] AMP03 difference amplifier datasheet,
http://www.farnell.com/datasheets/98408.pdf

[78] A. Steffen , A. Alberti, W. Alt , N. Belmechria , S. Hild , M. Karski , A. Widera , and D. Meschede
Digital atom interferometer with single particle control on a discretized space-time geometry,
PNAS , 109 (25) 9770-9774, 2012

[79] J. Du, L. Hu, Y. Wang, J. Wu, M. Zhao, , D. Suter,
Experimental Study of the Validity of Quantitative Conditions in the Quantum Adiabatic Theorem,
Phys. Rev. Lett. 101, 060403 , 2008

[80] T. Albash, D. A. Lidar,
Adiabatic Quantum Computing,
https://arxiv.org/pdf/1611.04471.pdf

[81] H. J. Metcalf, P. van der Straten,
Laser cooling and trapping ,
Springer, 1999

[82] M. Mudrich, S. Kraft, K. Singer, R. Grimm, A. Mosk, M. Weidemüller,
Sympathetic Cooling with Two Atomic Species in an Optical Trap,
Phys. Rev. Lett. 88, 253001 ,2002

[83] M. H. Al-Hashimi , U.-J. Wiese,
Minimal Position-Velocity Uncertainty Wave Packets in Relativistic and Non-relativistic Quantum Mechanics,
Annals of Physics Vol.324, Iss. 12, 2009, Pages 2599-2621,
https://arxiv.org/pdf/0907.5178.pdf

[84] A. M. Rey, G. Pupillo, C. W. Clark, C. J. Williams,
Ultracold atoms confined in an optical lattice plus parabolic potential: A closed-form approach,
Phys. Rev. A 72, 033616 ,2005

[85] I. Bloch, J. Dalibard, W. Zwerger,
Many-body physics with ultracold gases,
Reviews of modern physics, Vol. 80, 2008

[86] M. H. S Amin, V. Choi,
First-order quantum phase transition in adiabatic quantum computation,
Physical Review A 80 (6), 062326, 2009

[87] W. R. Inc., Mathematica, Version 11.3, Champaign, IL, 2018.

[88] M. Köhl, H. Moritz, T. Stöferle, K. Günter, T. Esslinger,
Fermionic Atoms in a Three Dimensional Optical Lattice: Observing Fermi Surfaces, Dynamics, and Interactions,
Phys. Rev. Lett. 94, 080403 , 2005

[89] W Tschischik, R Moessner, M. Haque,
Breathing mode in the Bose-Hubbard chain with a harmonic trapping potential,
Phys. Rev. A 88, 063636 , 2013

[90] D. J. Griffiths,
Introduction to Quantum mechanics,
Pearson Prentice Hall, 2nd edition, 2004